



# Syn-Emplacement Fracturing in the Sandfell Laccolith, Eastern Iceland—Implications for Rhyolite Intrusion Growth and Volcanic Hazards

Tobias Mattsson<sup>1\*</sup>, Steffi Burchardt<sup>1,2</sup>, Bjarne S. G. Almqvist<sup>1</sup> and Erika Ronchin<sup>1,2</sup>

<sup>1</sup> Department of Earth Sciences, Uppsala University, Uppsala, Sweden, <sup>2</sup> Center for Natural Hazards and Disaster Science, Uppsala University, Uppsala, Sweden

## OPEN ACCESS

### Edited by:

Shanaka L. de Silva,  
Oregon State University, United States

### Reviewed by:

Alessandro Tibaldi,  
Università degli studi di Milano  
Bicocca, Italy  
Ben Matthew Kennedy,  
University of Canterbury, New Zealand

### \*Correspondence:

Tobias Mattsson  
tobias.mattsson@geo.uu.se

### Specialty section:

This article was submitted to  
Volcanology,  
a section of the journal  
Frontiers in Earth Science

**Received:** 11 November 2017

**Accepted:** 17 January 2018

**Published:** 05 February 2018

### Citation:

Mattsson T, Burchardt S,  
Almqvist BSG and Ronchin E (2018)  
Syn-Emplacement Fracturing in the  
Sandfell Laccolith, Eastern  
Iceland—Implications for Rhyolite  
Intrusion Growth and Volcanic  
Hazards. *Front. Earth Sci.* 6:5.  
doi: 10.3389/feart.2018.00005

Felsic magma commonly pools within shallow mushroom-shaped magmatic intrusions, so-called laccoliths or cryptodomes, which can cause both explosive eruptions and collapse of the volcanic edifice. Deformation during laccolith emplacement is primarily considered to occur in the host rock. However, shallowly emplaced laccoliths (cryptodomes) show extensive internal deformation. While deformation of magma in volcanic conduits is an important process for regulating eruptive behavior, the effects of magma deformation on intrusion emplacement remain largely unexplored. In this study, we investigate the emplacement of the 0.57 km<sup>3</sup> rhyolitic Sandfell laccolith, Iceland, which formed at a depth of 500 m in a single intrusive event. By combining field measurements, 3D modeling, anisotropy of magnetic susceptibility (AMS), microstructural analysis, and FEM modeling we examine deformation in the magma to constrain its influence on intrusion emplacement. Concentric flow bands and S-C fabrics reveal contact-parallel magma flow during the initial stages of laccolith inflation. The magma flow fabric is overprinted by strain-localization bands (SLBs) and more than one third of the volume of the Sandfell laccolith displays concentric intensely fractured layers. A dominantly oblate magmatic fabric in the fractured areas and conjugate geometry of SLBs, and fractures in the fracture layers demonstrate that the magma was deformed by intrusive stresses. This implies that a large volume of magma became viscously stalled and was unable to flow during intrusion. Fine-grained groundmass and vesicle-poor rock adjacent to the fracture layers point to that the interaction between the SLBs and the flow bands at sub-solidus state caused the brittle-failure and triggered decompression degassing and crystallization, which led to rapid viscosity increase in the magma. The extent of syn-emplacement fracturing in the Sandfell laccolith further shows that strain-induced degassing limited the amount of eruptible magma by essentially solidifying the rim of the magma body. Our observations indicate that syn-emplacement changes in rheology, and the associated fracturing of intruding magma not only occur in volcanic conduits, but also play a major role in the emplacement of viscous magma intrusions in the upper kilometer of the crust.

**Keywords:** laccolith, cryptodome, magma flow, intrusion emplacement, strain localization, magma degassing, volcanic hazards

## INTRODUCTION

Deformation related to laccolith emplacement has generally been considered to be focused in the host rock, and therefore the host-rock properties are assumed to control laccolith growth (e.g., Pollard and Johnson, 1973; Jackson and Pollard, 1988; Kerr and Pollard, 1998; Bungler and Cruden, 2011). However, relict cryptodomes display extensive concentric internal deformation, including brecciated carapace and strong flow-banding and partially brecciated rims (Snyder and Fraser, 1963; Goto and McPhie, 1998; Goto et al., 2000, 2004; Stewart and McPhie, 2003). The Miocene rhyolitic Sandfell laccolith intruded the flank lava-succession of the Reydarfjörður central volcano at a depth of ~500 m (Hawkes and Hawkes, 1933; Gibson, 1963; Gibson et al., 1966; Martin et al., 2011; de Jesus Padilla, 2015), and can therefore be considered a cryptodome. Cryptodomes and laccoliths are sub-surface, dome-shaped magma intrusions that uplift and deform their host rocks (Gilbert, 1877; Minakami et al., 1951; Lipman et al., 1981). While a laccolith may form down to depths of ~3–4 km in the crust, the intrusion can be called a cryptodome if it intrudes a volcanic edifice or close to the surface (cf. Gilbert, 1877; Minakami et al., 1951; Pollard and Johnson, 1973; Corry, 1988; Roni et al., 2014). During cryptodome emplacement, the push of the intruding magma destabilizes the volcanic edifice, which may lead to edifice collapse and explosive eruption (e.g., Lipman et al., 1981; Donnadieu et al., 2001). Laccolith/cryptodome intrusion events have been documented at Mt. St. Helens, USA, Cordon Caulle, Chile, and Usu, Japan, where intrusion time scales range from a month to approximately a year (Minakami et al., 1951; Lipman et al., 1981; Castro et al., 2016). The geological record and geochronology of exposed laccoliths also display incremental growth histories ranging over thousands of years (e.g., Michel et al., 2008).

Structures within cryptodomes have been suggested to be generated by the dynamic interplay between intrusive and thermal stresses (Goto and McPhie, 1998; Goto et al., 2000, 2004; Stewart and McPhie, 2003), but the processes leading to, and the effects of brittle deformation on cryptodome emplacement have not been studied in detail. On the other hand, brittle deformation in magma moving through volcanic conduits has been shown to be a manifestation of strain-induced ductile-brittle transition and to regulate the eruptive behavior of magma by influencing its potential to degas (Gonnermann and Manga, 2003; Tuffen et al., 2003; Lavallée et al., 2007; Cordonnier et al., 2012; Kendrick et al., 2013, 2016; Ashwell et al., 2015; Pistone et al., 2016; Kushnir et al., 2017). Fracturing, for example, decompresses the magma locally and creates permeability, which promotes degassing and affects the rheological behavior of magma (Nara et al., 2011; Castro et al., 2012; Pistone et al., 2013; Heap and Kennedy, 2016; Kushnir et al., 2017). This highlights the potential importance of magma deformation during intrusion emplacement.

The preferred orientation of minerals, or fabric, in igneous rocks can be used to study magma flow and the processes that occur during intrusion emplacement (e.g., Benn and Allard, 1989; Paterson et al., 1998). Several different analytical methods have been used to decipher the mineral fabric in magmatic intrusions, e.g., the use of a petrographic microscope equipped

with a universal stage (e.g., Brothers, 1964; Žák et al., 2005), neutron diffraction goniometry (Silva et al., 2014), electron backscatter diffraction (EBSD) (Holness et al., 2012), and anisotropy of magnetic susceptibility (AMS) (Knight and Walker, 1988; Geoffroy et al., 2002; Žák et al., 2005; de Saint-Blanquat et al., 2006; Stevenson et al., 2007; Horsman et al., 2009; Eriksson et al., 2011; Payacán et al., 2014; Roni et al., 2014; McCarthy et al., 2015). Crystallographic preferred orientation (CPO) and shape preferred orientation (SPO) are often analyzed with oriented thin sections and require distinct crystal boundaries (e.g., Benn and Allard, 1989; Paterson et al., 1998; Geoffroy et al., 2002; Horsman et al., 2009; Payacán et al., 2014). EBSD and neutron diffraction goniometry are powerful tools to analyze CPO and SPO in rock, but tend to be time-consuming and are therefore not favored for large sample sets (e.g., Prior et al., 1999). In contrast, AMS defines the orientation and magnitude of magnetic susceptibility of a material in an applied weak magnetic field, which is usually determined by the orientation of the ferromagnetic mineral in rocks (e.g., Borradaile and Jackson, 2010). However, all minerals contribute to the magnetic susceptibility in a rock, and when there are very little ferromagnetic minerals, other minerals will contribute to the signal. An advantage of AMS analysis is the possibility to rapidly determine the 3D fabric for a large sample set on regional scales.

In viscous magma intrusions, the emplacement-related magmatic fabrics are commonly concentric and reflect the shape of the magma body (e.g., de Saint-Blanquat et al., 2006; Stevenson et al., 2007; Payacán et al., 2014; McCarthy et al., 2015). Therefore, the magmatic fabrics have been interpreted as due to divergent flow in the magma body or by compaction against the magma body roof and wall (e.g., Paterson et al., 1998; Buisson and Merle, 2004). In magmatic sheet intrusions, such as dykes, magmatic fabrics are often imbricated due to wall shear (e.g., Knight and Walker, 1988; Geoffroy et al., 2002; Cañón-Tapia and Herrero-Bervera, 2009; Eriksson et al., 2011). To complement magma fabric analyses, Paterson et al. (1998) suggested to also analyze microstructures to determine the state of the magma when the fabric developed and its relationship to other structures in the rock. In order to understand the interplay between emplacement and deformation of intruding magma in laccoliths and cryptodomes, we investigate magma flow, rheological changes, and deformation in the Sandfell laccolith using field observations, measurements of flow indicators, microstructural analysis, AMS, FEM modeling and a 3D structural model.

## The Sandfell Laccolith

The fjords of eastern Iceland expose several extinct and eroded volcanic systems that consist of central volcanoes and fissure swarms (Walker, 1963; Gibson et al., 1966). The 11.7 Ma Sandfell laccolith is situated in Fáskrúðsfjörður (**Figure 1A**) and composed of a feldspar- and quartz-phyric rhyolite (Martin and Sigmarsson, 2010; de Jesus Padilla, 2015). The Sandfell laccolith intruded along, and inflated within, an ~30 m thick ignimbrite layer (named T2) in the Neogene lava-pile (**Figure 2**) (Hawkes and Hawkes, 1933; Gibson, 1963; Gibson et al., 1966). The intrusion depth was determined to ~540 m below the paleo-surface by measuring the thickness of the up-domed

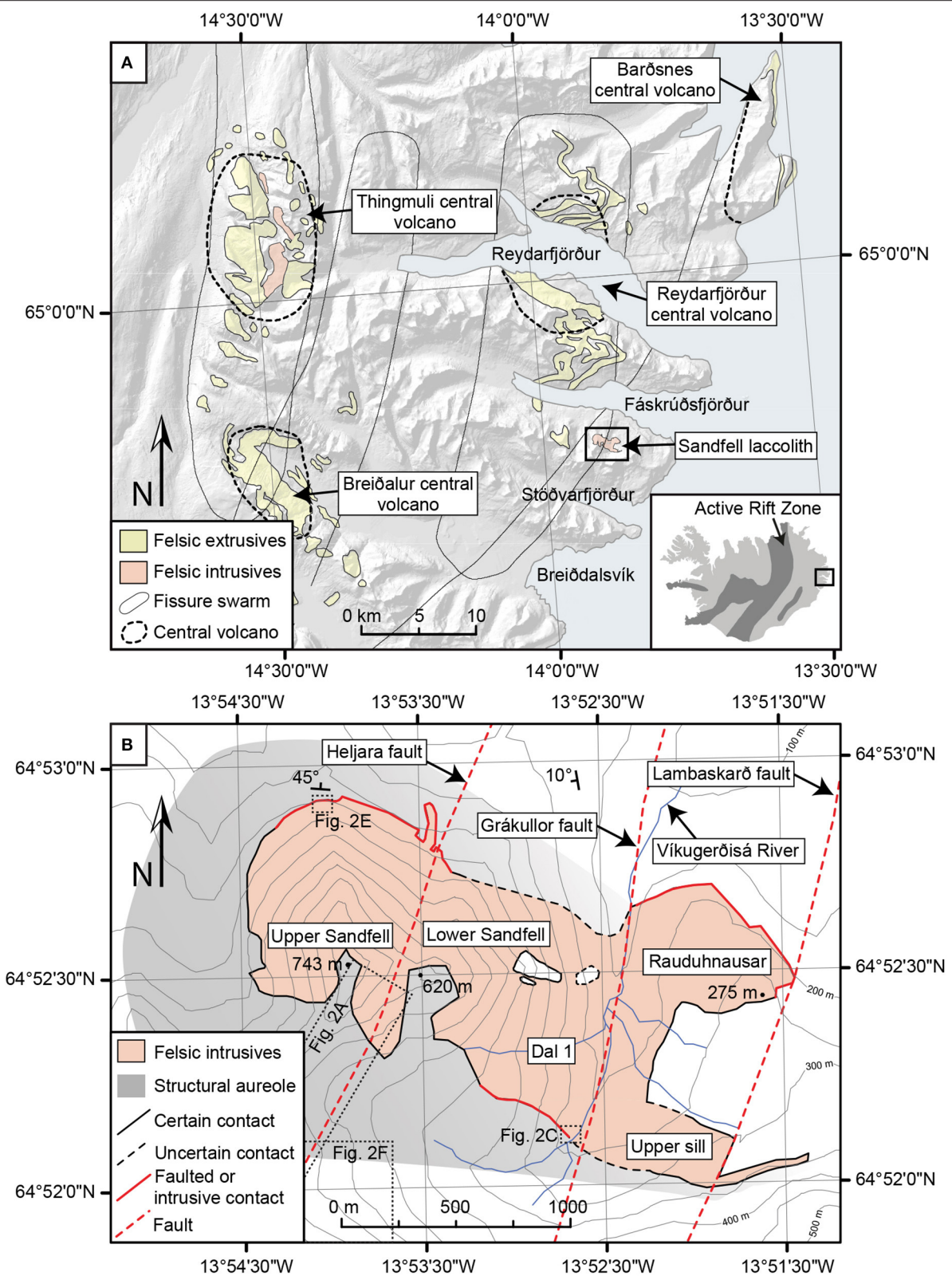


**FIGURE 1 | (A)** Map of locations of exposed fissure swarms and central volcanoes in the East fjords of Iceland (based on data from National Land Survey of Iceland, <http://www.lmi.is/wp-content/uploads/2013/10/License-for-use-of-free-NLSI-data-General-Terms.pdf>). **(B)** Map of the Sandfell laccolith. The structural aureole includes the country rock that is folded, rotated, faulted, and fractured by the emplacement of the Sandfell laccolith. The structural aureole is less pronounced in the eastern part of the laccolith (shown by the gray gradient). Stippled boxes show locations of images in **Figures 2A,C,E,F**.

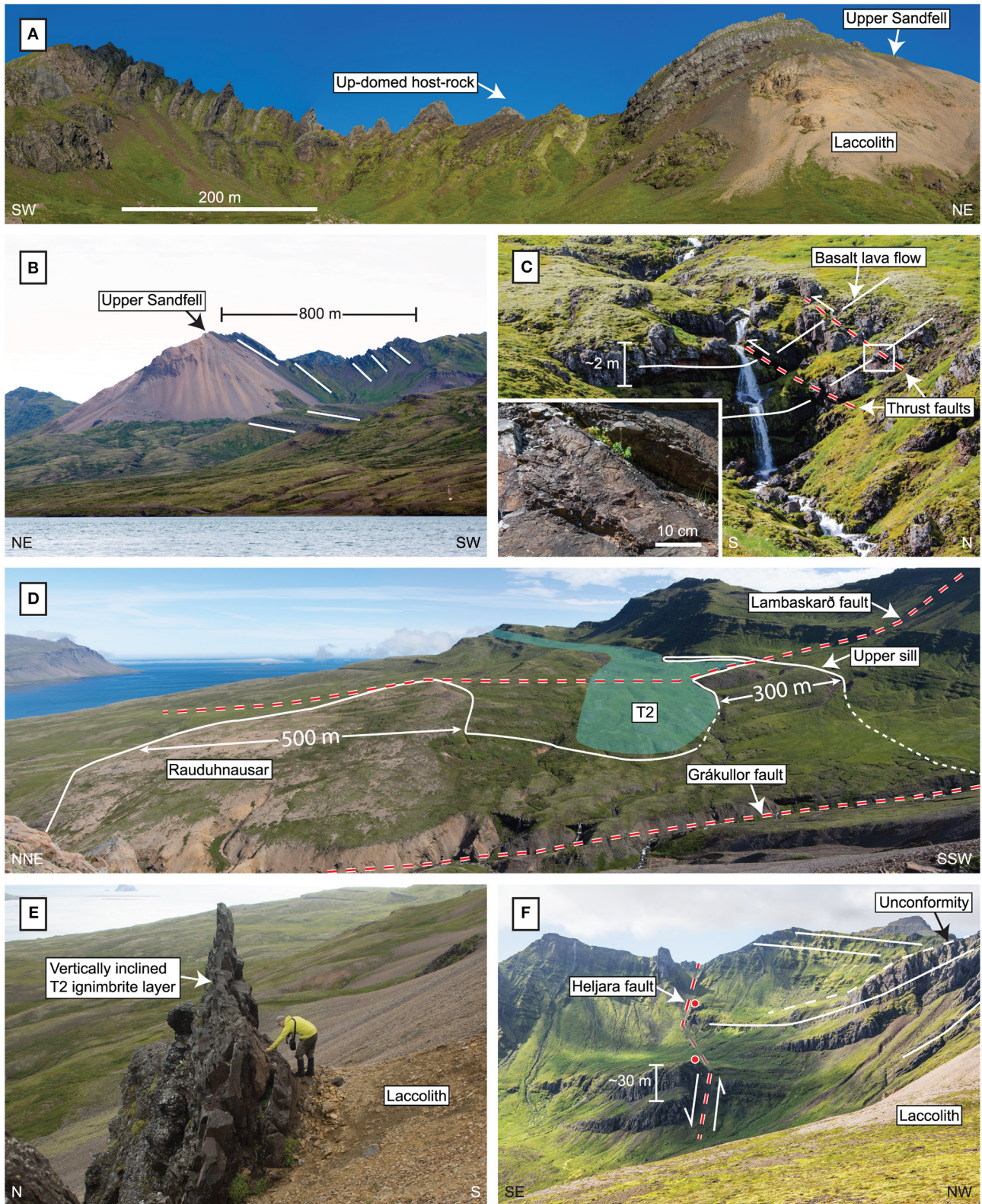


**FIGURE 2 | (A)** Photo of basaltic lavas (dark rock) and silicic pyroclastic (light rock) layers up-domed by the emplacement of the Sandfell laccolith. Image location is given in **Figure 1B**. **(B)** View from the northern shore of Fáskrúðsfjörður looking toward the SE and the Sandfell laccolith. Note the differences in dip between the lava pile in front of the laccolith and the lava pile next to the laccolith. **(C)** View toward west and a discrete kink (monocline) in the basalt host rock that marks the

(Continued)

**FIGURE 2** | transition from undeformed to deflected lava pile, ~300 m south of the laccolith. The dashed lines mark thrust faults in the lava pile domed by the emplacement of the Sandfell laccolith. Inset photo shows detailed view of a fault plane. The lava flows are ~2 m thick. Image location is given in **Figure 1B**. **(D)** View east from the main body of the laccolith toward the sill-like rhyolite lobes, Rauduhnausar and the Upper sill. The Upper sill crops out within the T2 ignimbrite, while the rest of the laccolith is exposed below the lowermost unit of the ignimbrite. **(E)** Contact between the laccolith and the deflected, almost vertically inclined glassy T2 ignimbrite, north of Upper Sandfell. Person for scale. Image location is given in **Figure 1B**. The photo was included in this publication with written consent from the person in the photo. **(F)** View south from the main body of the laccolith (top of Lower Sandfell) toward the Neogene lava pile. The layering of the different lava flows is marked with white solid lines. Note the unconformity between the deformed host rock and younger basalt lava flows marked by the white dashed line. The vertical displacement on the Heljara fault is ~75 m and is indicated by the two red dots (Gibson, 1963). Image location is given in **Figure 1B**.

host-rock that unconformably underlies younger lavas and pyroclastic rocks unaffected by the laccolith (**Figure 2F**; Hawkes and Hawkes, 1933). The up-domed host-rock consists primarily of basalt lava flows, but also a ~30 m thick rhyolitic andesite lava flow and a ~10 m thick felsic tuff (T3) (Hawkes and Hawkes, 1933; Gibson, 1963; Gibson et al., 1966). The Sandfell laccolith may also be the source of a felsic tuff that crops out between the domed and younger undeformed lavas, the so-called Sandfell tuff (Hawkes and Hawkes, 1933; Gibson, 1963; Gibson et al., 1966). The absence of compositional heterogeneities, internal contacts, and mafic enclaves within the Sandfell laccolith (Hawkes and Hawkes, 1933) indicates that the Sandfell laccolith formed by the intrusion of a single pulse or by the rapid succession of several continuous pulses of magma. Three regional normal faults, the Heljara, Grákullor, and Lambaskarð faults, cut and displace the laccolith body (**Figures 1B, 3**). See Supplementary Informations 1, 2 for a detailed geological background of the Sandfell laccolith.

## METHODS

### Field Campaign and Samples

In August 2016, we collected 50 oriented samples for AMS and microstructural analysis, distributed over the laccolith. The sampling locations strongly depended on the availability of outcrops. The *in-situ* orientation of each sample was measured with a Freiburger stratum compass and marked on the sample. Sample location and elevation were recorded in the coordinate system UTM zone 28N with a handheld GPS. Various types of magma flow indicators or magmatic fabric were measured in the field (including flow banding, mineral alignments) with a smartphone and the Fieldmove Clino™ application (<https://www.mve.com/digital-mapping/>). The digital compass measurements were regularly checked with an analog compass. At every sample locality, several measurements of the *in-situ* fabric were collected and averaged. All orientation measurements were corrected for the local compass declination of  $-10^\circ$ . We also mapped contacts to the host rock and emplacement-related features, such as faults.

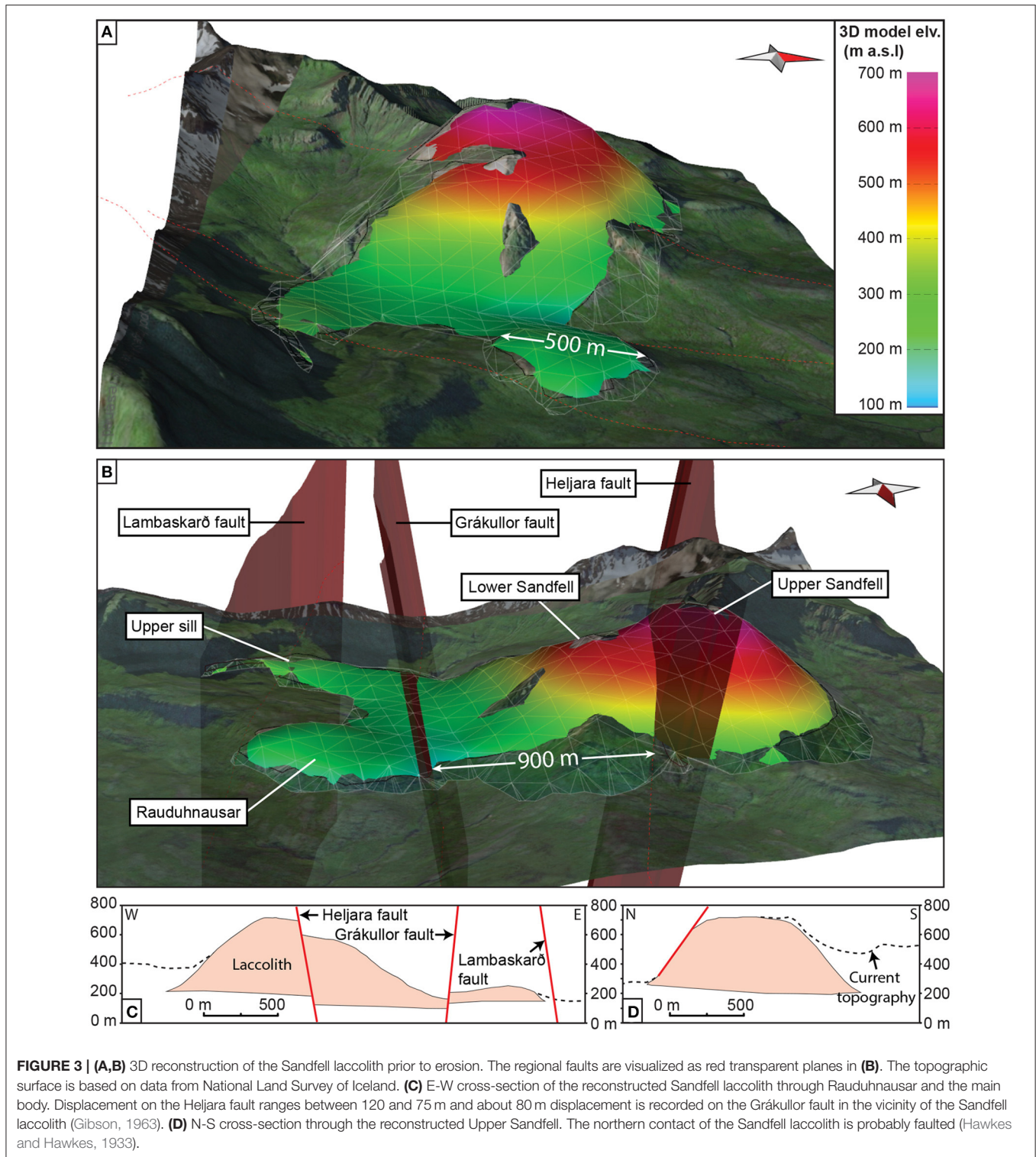
### Microstructural Analysis

Thin sections oriented perpendicular and parallel to flow bands were prepared from representative samples from different areas of the Sandfell laccolith to analyze the magmatic deformation features in the rhyolite. Ten samples were analyzed by creating photo mosaics of thin section images in Adobe® Photoshop®. The photo mosaic images were oriented by rotating flow bands to the horizontal and were then imported into the geological data

visualization and analysis software MOVE™ by Midland Valley Ltd. The orientations of deformation features were analyzed by manually marking lineaments with the Line tool in MOVE™. The crystal and vesicle content in the samples were estimated by manually drawing polygons on crystals with observable crystal faces (crystals  $\geq 50 \mu\text{m}$  in diameter) and calculating their cumulative area.

### Three-Dimensional Model and Laccolith Volume Calculation

A digital elevation model (DEM) of Fáskrúðsfjörður (50 m resolution, is\_50v\_haederlikan, Landmælingar, Ísland, based on data from the National Land Survey of Iceland, <http://www.lmi.is/wp-content/uploads/2013/10/License-for-use-of-free-NLSI-data-General-Terms.pdf>) was imported into MOVE™. The mapped contact was drawn onto the topographic surface, and contact measurements were projected as surfaces down-dip from the contact. The T2 ignimbrite was assumed to represent the bottom surface of the laccolith and its location was estimated by using the Neogene lava pile dip, the exposure of T2 from the geological map of the Reydarfjörður central volcano (Gibson et al., 1966), and the topographical surface. Displacement on the regional faults was taken into account when estimating the location of the floor of the intrusion (see **Figure 3C**; Supplementary Information 2). A 3D model for calculating the volume of magma in the Sandfell laccolith was produced using 20 cross-sections cutting the laccolith in an E-W (spacing 140 m) and N-S (spacing 260 m) direction. The trace of the contacts was extrapolated manually with the Line tool in MOVE™ from the contact to the assumed floor (T2) and roof of the laccolith in the cross-sections. The roof contact surface was generated using the cross-section contact lines and the present-day contacts to the host rock with Ordinary kriging (see Supplementary Information 3). A volume was created with the Tetravolume tool in MOVE™ between the roof and floor surfaces of the laccolith. Uncertainties in estimating the volume of the Sandfell laccolith by using 3D cross-section reconstruction is introduced by the accuracy of the DEM and the horizontal precision of the mapped contacts to the Sandfell laccolith and the T2 ignimbrite. Furthermore, because the floor of the Sandfell laccolith is not exposed, we do not know if it is flat, convex, or concavely bulging. To avoid overestimating the volume of the Sandfell laccolith, we assumed that the floor of the intrusion is flat and that the eroded roof was located in general <50 m from the exposed surface of the present-day exposed parts of the Sandfell laccolith. However, since the contacts and the intrusion horizon of the Sandfell laccolith are generally well-constrained



by previous mapping and mapping carried out during this study (see e.g., **Figures 1B, 2A,D,E**; Hawkes and Hawkes, 1933; Gibson et al., 1966), the calculated volume of the Sandfell laccolith can be assumed as a precise estimation of the minimum intrusion volume.

### AMS Analysis

The 50 samples collected during field work were prepared for AMS analysis at Uppsala University. Between 5 and 12 cores, 21 mm long × 24 mm in diameter, were extracted from each sample, resulting in a total of 387 cores from the 50 original

samples. The symmetric magnetic susceptibility tensor of each core was measured in semi-automatic spinning mode with an Agico Kappabridge MK1-FA at the Laboratory for Experimental Palaeomagnetism at the Department of Earth Sciences, Uppsala University. The eigenvalues and eigenvectors were calculated from the susceptibility tensor, and they are represented by the three orthogonal, principal axes of susceptibility,  $k_1 \geq k_2 \geq k_3$ . The average magnetic susceptibility ( $K_m$ ) was calculated for every sample using the arithmetic mean of the principal susceptibility axes (Equation 1):

$$K_m = \frac{k_1 + k_2 + k_3}{3} \quad (1)$$

The principal axes of susceptibility are used to analyze magnetic fabric or essentially the prevailing orientations of the dominant magnetic minerals. The magnetic susceptibility principal axes,  $k_1$ ,  $k_2$ , and  $k_3$  can be represented by an ellipsoid, with magnitude and orientation (Khan, 1962). The AMS in a rock can be further described by the parameters  $P_j$  and  $T$ , as originally defined by Jelínek (1981). The corrected degree of anisotropy ( $P_j$ ) is given by Equation (2),

$$P_j = \exp \sqrt{2((\eta_1 - \eta_m)^2 + (\eta_2 - \eta_m)^2 + (\eta_3 - \eta_m)^2)} \quad (2)$$

where  $\eta_x = \ln(k_x)$ ,  $x = 1, 2, 3$  and  $\eta_m = \sqrt[3]{\eta_1 \eta_2 \eta_3}$ . The shape factor ( $T$ ) describes the shape of the ellipsoid and is given by Equation (3),

$$T = \frac{2\eta_2 - \eta_1 - \eta_3}{\eta_1 - \eta_3} - 1 \quad (3)$$

We have adopted the following scheme to define the strength of the bulk susceptibility and shape of the magnetic fabric of the samples. When  $K_m > 5 \times 10^{-4}$  [SI], the bulk magnetic susceptibility is considered moderate to strong, and when  $K_m < 5 \times 10^{-4}$  [SI], the sample bulk magnetic susceptibility is considered weak.  $T = 1$  to 0.15 represent a dominantly oblate fabric (foliation),  $T = -0.15$  to  $-1$  a dominantly prolate fabric (lineation) and  $T = \pm 0.15$  a triaxial neutral fabric. A sample with triaxial (neutral) symmetry of the magnetic susceptibility ellipsoid may not have a distinct type of magmatic fabric or it might represent oblate and prolate fabrics that are superimposed on each other (e.g., Hrouda and Ježek, 1999).

We analyzed the Curie temperatures of the ferromagnetic minerals in the Sandfell rhyolite in order to resolve which magnetic minerals are primarily responsible for the magnetic susceptibility. Six samples (four showing minor alteration and two distinctly altered) were crushed in a Jaw crusher and milled to fine powders in an Agate mill. Magnetic phases were separated from the powders using a magnet. The susceptibility of the magnetic separates was measured while heated in the MK1-FA, from room temperature to 700°C and subsequently cooled to room temperature again.

The dip and azimuth of an oblate magnetic susceptibility fabric was calculated by fitting a plane to the average  $k_1$  and  $k_2$

axes of a sample. The trend and plunge of the  $k_1$  axis represent the magnetic lineation for prolate fabrics. At localities where the magnetic fabric is triaxial, both the magnetic foliation and lineation were considered for interpretation of the magmatic fabric. Techniques to determine magma flow direction from only the AMS fabric were not tested (cf. Cañón-Tapia and Herrero-Bervera, 2009 and references therein). The emplacement-related fabrics of the magma were interpreted by comparing the orientations of the magmatic and the magnetic fabric. When the two measured fabrics did not correlate, we used the following guiding principles: (i) In samples with weak bulk magnetic susceptibility and dissimilar magmatic and magnetic fabric, only the *in situ* measured magmatic fabric was used as an indication of the flow and fabric shape of the magma, since the magnetic fabric could have been affected by hydrothermal alteration; (ii) where the bulk magnetic susceptibility is considered moderate to strong ( $K_m > 5 \times 10^{-4}$  [SI]), both the AMS and measured fabric were considered to represent fabrics created during the emplacement of the magma. Magnetic fabric distribution in the Sandfell laccolith was analyzed with the surface analysis software Surfer® from Golden Software. The magnetic fabric distribution in the Sandfell laccolith was contoured with Ordinary kriging using samples with moderate to strong bulk magnetic susceptibility. UTM location (XY) and the average  $T$  shape factor as Z were used as input for each sample.

## Finite Element Modeling

The COMSOL Multiphysics v5.3a software (<http://www.comsol.com>) was used to model the cooling of a magma body of Sandfell-laccolith dimensions with a Finite Element Method (FEM) model. The FEM model is axisymmetric and built over a cylindrical coordinate system, with negative  $z$ -values corresponding to depths below sea level. The modeled magma reservoir is oblate, 500 m high and 700 m long, and has a roof located at 500 m depth. The computational domain corresponds to a section of the crust of 10 km radius, extending to 10 km below sea level. The domain is partitioned into about 30,000 linear triangular elements having up to 2 m size near the edges of the reservoir and 250 m size at the far-field boundary. For the initial temperature profile of the host rock, we used a typical geothermal gradient of Iceland (Flóvenz and Saemundsson, 1993) with uniform lateral temperature profile. The far-field is considered to have no heat flux (i.e., the host rock in the far-field is insulated).

## RESULTS

### Shape and Volume of the Sandfell Laccolith

The main body of the Sandfell laccolith is dome-shaped and has two peaks, Upper and Lower Sandfell, both covered by a thin roof of sub-horizontal lavas. The laccolith is most prominent at Upper Sandfell (~740 m a.s.l.) in the western part of the intrusion, while Lower Sandfell forms a plateau at ~620 m a.s.l. in the central region of the laccolith (Figures 3A,B). The eastern part of the main body of the laccolith is connected to two marginally inflated rhyolite “sills” called Rauduhnausar and the Upper sill (Figures 2D, 3A,B). The laccolith body is at its maximum ~500 m thick, ~2700 m long and ~1400 m wide,

resulting in an aspect ratio of length = 5.4: width = 2.8: height = 1. The estimated pre-erosional volume of the Sandfell laccolith is at least  $0.57 \text{ km}^3$ . The volume of Sandfell laccolith compares with that of felsic lava flows in the eastern fjords, which range from  $0.3$  to  $2.5 \text{ km}^3$  (Walker, 1966). After its emplacement the entire laccolith has been gently tilted toward the active rift in Iceland together with the surrounding lava pile (Walker, 1958, 1963, 1974).

## Contact Relationships

Most of the contacts between the host rock and the Sandfell laccolith are covered by scree, but can be well-constrained by distinct host-rock deflection. The exposed contacts are generally concordant (i.e., parallel to the layering of the lava pile) (Figures 1, 2A,B; see also Hawkes and Hawkes, 1933). However, the south-east flank of Lower Sandfell has partly deflected and punched (faulted) the host-rock lavas (cf. Corry, 1988), and in north-western Rauduhnausar, the contact is stepped and intrusive, i.e., discordant to the host-rock layering, but follows the joint system in the basalt host rock. A discrete kink marks the transition from undeformed to deflected host rock (Figure 2C). Reverse and normal faults have accommodated some of the uplift associated with laccolith emplacement in the deflected host rock (Figure 2C). However, the bulk of the  $\sim 500 \text{ m}$  of stretching of the host-rock lavas required to accommodate the rhyolite magma was probably achieved through the formation of a fault along the northern flank of the Sandfell laccolith (Hawkes and Hawkes, 1933; Figure 3D). Additionally, no hydrothermal system has been observed in the host rock to the Sandfell laccolith.

The intrusion horizon of the Sandfell laccolith, the T2 ignimbrite (Tuff 2 of the Reydarfjörður central volcano, Figures 2D,E), was erupted from a vent situated  $\sim 10 \text{ km}$  north of the Sandfell laccolith (Gibson, 1963). T2 has three texturally different sub-units, which are exposed at different localities surrounding the laccolith. The lowermost unit of the ignimbrite is unconsolidated (un-welded), red to pale yellow and greenish-blue in color. The middle unit is a glassy welded pitchstone that is, in turn, overlain by a welded platy fine-grained pale greenish-blue to red-purple unit. All units of the T2 ignimbrite contain feldspar phenocrysts and abundant angular basalt fragments. While the main body of the laccolith and Rauduhnausar intruded below the lowermost unconsolidated unit of the ignimbrite, the Upper sill is exposed in between the lowermost unit and the upper welded units. The textural boundaries within the ignimbrite were likely exploited by the rhyolite magma during intrusion. The arrangement of the two offshoots also indicates that the rhyolite magma intruded eastwards from the main body in two lobes into different levels of the T2 stratigraphy (Figure 2D), forming a Christmas-tree geometry (cf. Corry, 1988).

## Magmatic Fabric

The Sandfell rhyolite consists of euhedral plagioclase phenocrysts in a fine-grained cryptocrystalline groundmass (crystals  $< 50 \mu\text{m}$  in length) of wispy anhedral alkali feldspar, plagioclase, quartz, and opaque oxide phases (Figure 4). Anhedral to

subhedral quartz also occurs as a second “phenocryst” phase, although crystals are smaller compared to the plagioclase (Figures 4C,D, 6). Vesicles in the Sandfell rhyolite are dominantly rounded ( $\sim 100 \mu\text{m}$  in diameter), but also display elongate shapes (up to  $1 \text{ mm}$  across,  $1\text{--}5 \text{ mm}$  long). Mineral and vesicle alignments and mm- to cm-wide bands of varying color occur pervasively within the Sandfell laccolith (Figures 5A,B), providing indicators of magma flow (magmatic fabric). The intensity of the magmatic fabric varies within the laccolith, ranging from crystal alignments to distinct flow banding (Supplementary Table 1). The rhyolite is commonly platy, in particular close to the contact with the host rock, and parts parallel to the magmatic fabric. Two types of flow banding were identified in the Sandfell rhyolite: (i) Flow bands composed of several thin bands of aligned quartz crystals ( $\sim 100 \mu\text{m}$  in diameter) and occasional plagioclase phenocrysts, and (ii) flow bands caused by small-scale variations in groundmass crystallinity and vesicle shape (rounded to elongate) and content (between  $0$  and  $\sim 2\%$ ) (Figures 4B–D, 6). The samples from the eastern and lower exposed parts of the Sandfell laccolith (Dal 1 and Rauduhnausar) are generally devoid of vesicles. The Sandfell rhyolite contains on average  $6\%$  phenocrysts ( $> 50 \mu\text{m}$  in diameter,  $\sim 3\%$  plagioclase;  $3\%$  quartz), however, the crystal content can locally reach up to  $30\%$  in flow bands. In several samples with contact-parallel flow bands in the main body of the laccolith (Figure 7A), the phenocrysts and groundmass display an S-C fabric, where the flow bands are parallel to the C plane, and indicate shear (Figure 6). The acute angles between the S and C plane range from  $30$  to  $40^\circ$ .

In total 353 measurements of indicators of magma flow were collected in the Sandfell laccolith (Supplementary Table 2). The magmatic fabric is dominantly moderately- to steeply-dipping ( $84\%$  of measurement localities,  $> 35^\circ$ ) and generally oriented parallel to the laccolith contact (Figure 7A). The zone with contact-parallel measurements ranges from several hundreds of meters wide (from the contact) in the main body to a couple of meters wide in Rauduhnausar. Beyond the contact-parallel zone, the magmatic fabric azimuths are usually perpendicular to the contact, but displays local variation on meter scale (Figure 7A). The Dal 1 valley exposes the deepest section through the main laccolith body (Figure 1B). There, the flow banding is weak, and mineral alignment represents the main flow indicator, while flow bands are the main indicators elsewhere in the main body of the laccolith.

Flow indicators across the intrusion are overprinted by narrow zones of localized shearing, which we refer to as strain-localization bands (SLBs) (Figures 4C–E). Displacement along SLBs is up to  $2 \text{ mm}$  and accompanied by aligned crystal and groundmass mineral phases, and rarely elongate vesicles. The crystal alignment in the SLBs indicates that this shear deformation occurred in a magma or crystal mush where crystals could rotate, as opposed to during solid-state deformation, which would yield re-crystallization (cf. Paterson et al., 1989). Additionally, in the main body of the laccolith, the SLBs are oriented oblique to orthogonal to the flow bands and form conjugate sets with an acute bisector plane oriented at an average angle of  $77^\circ$  to the flow band (Figure 4C). Similar conjugate SLBs

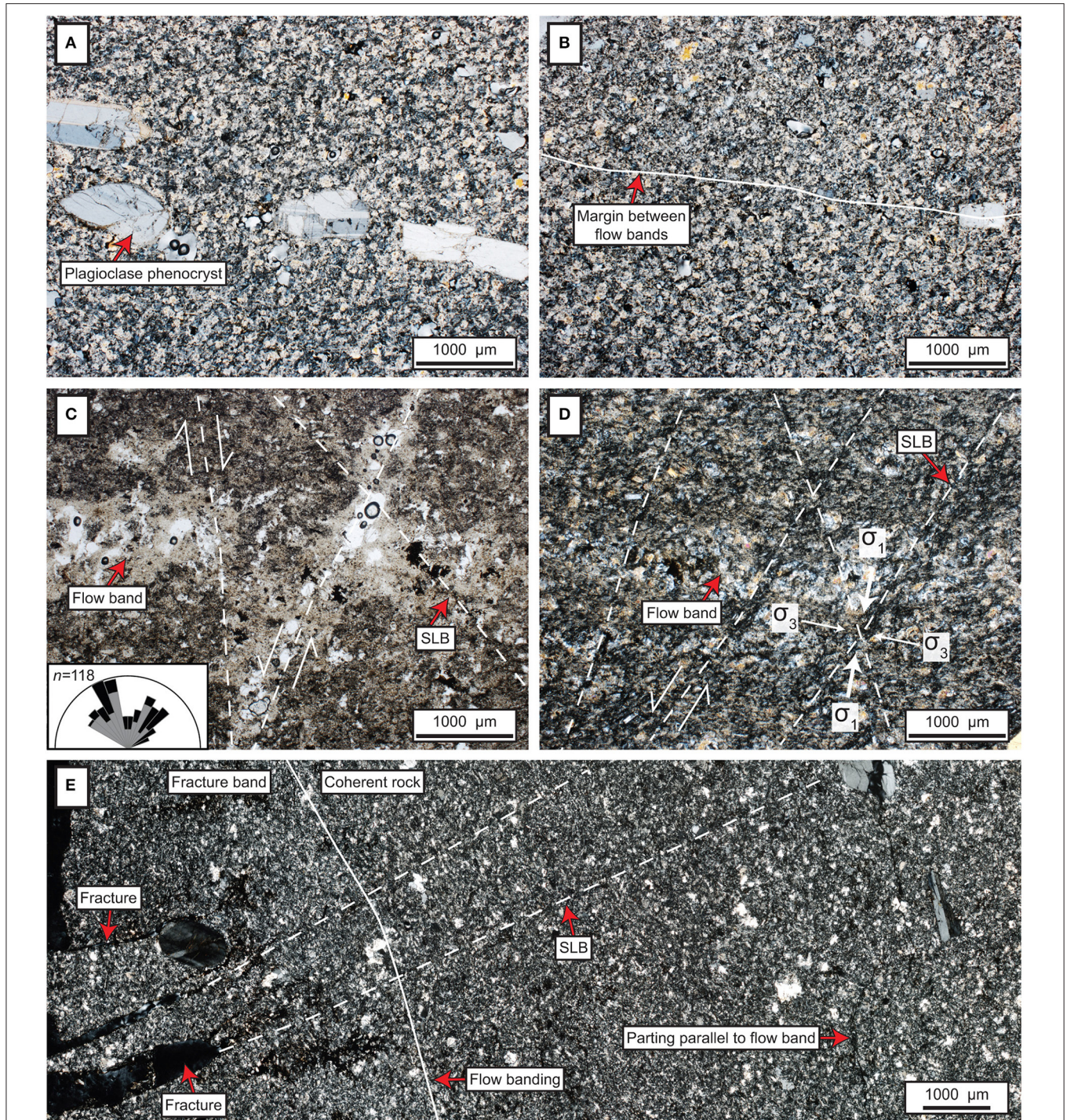


**FIGURE 4 | (A)** Microphotograph of aligned euhedral plagioclase phenocrysts in the Sandfell laccolith indicative of magma flow (crossed polars = CPL). **(B)** Microphotograph showing discrete variation in crystallinity in the rhyolite groundmass (CPL). The transition from fine-grained subhedral groundmass phases (bottom half of image) to dominantly anhedral crystal phases (top half of image) is marked by the white line. Crystals in the groundmass become increasingly anhedral with indistinct crystal boundaries adjacent to fracture bands. **(C)** Microphotograph of flow banding in sample close to the roof contact of Lower Sandfell (plane polarized = PPL). SLBs (indicated by dashed lines) displace the primary flow band. Inset shows orientations of SLBs in a bi-directional rose plot (black bars,  $n = 79$ ) and fracture orientations (gray bars,  $n = 39$ ) relative to flow bands. The acute angle of the conjugate SLBs is smaller in thin sections perpendicular to the strike of the flow bands. **(D)** Microphotograph of a flow band in the Sandfell rhyolite in a sample from SE of Upper Sandfell (CPL). The flow bands are characterized by variations in grain-size. The dark SLBs, some marked by white dashed lines, are oriented oblique to the flow banding. **(E)** CPL microphotograph of fracture band and rhyolite groundmass next to fracture bands. The strain-localization bands (SLBs) (white dashed lines) are observed to transition into fractures. Note the change in groundmass crystallinity and texture closer to the fracture band. All thin sections are oriented perpendicular to the strike or dip-direction of the flow bands.

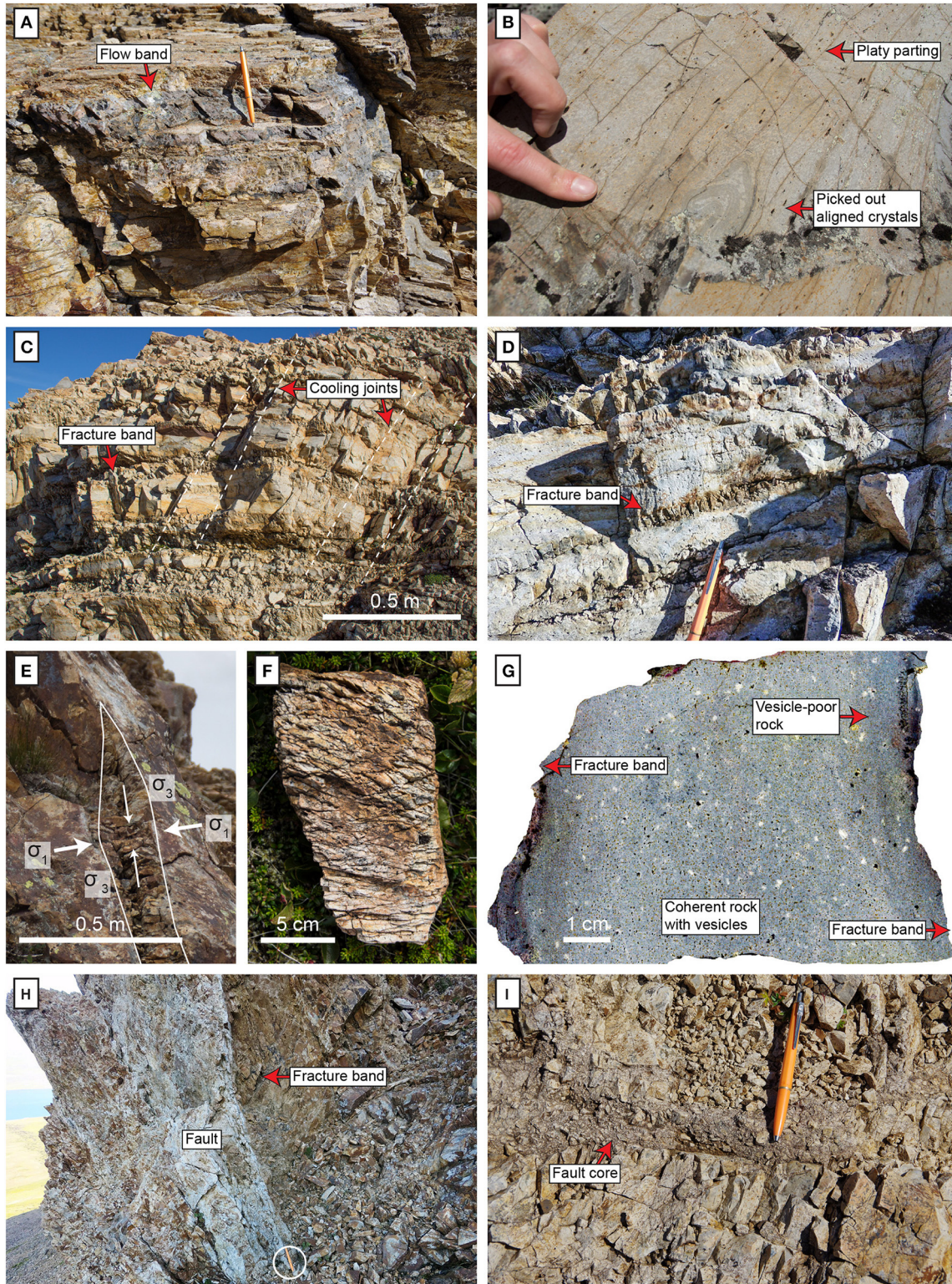


**FIGURE 5 | (A)** Flow bands in the Sandfell rhyolite on the southern slopes of Lower Sandfell. Flow bands are planes of varying color and crystallinity in outcrop and hand-specimen scale. The flow bands are not abundantly folded, which indicates that they were generated in the laccolith body as opposed to in the feeder. Pen for scale. **(B)** Flow fold and aligned hollows of picked-out crystals in rhyolite at Upper Sandfell. Note the platy parting parallel to the crystal alignment. **(C,D)** Fracture (Continued)

**FIGURE 5** | bands separated by coherent rock. The photo is from below Lower Sandfell in the main body of the laccolith. The fracture bands consist of multiple fractures that are oblique to orthogonal to the strike of the bands. Some of the fractures in the bands are rotated. Wider-spaced cooling joints cut both the fracture bands and coherent rock at a consistently-oblique angle to the strike of the bands (marked by white dashed lines). Pen for scale in **(D)**. Notably, different degrees of fragmentation are observed in the Sandfell laccolith that range from arrays of several-cm-spaced fractures in vesicle-rich parts of the rock, through fully developed fracture bands, to rotated fractures in the fracture bands, to breccia. **(E)** Tip of a fracture band in the NW-part of the Sandfell laccolith. Maximum ( $\sigma_1$ ) and minimum ( $\sigma_3$ ) principal stress directions are indicated on the photo as suggested by microstructural analysis on the fractures in the fracture bands. **(F)** Plane-parallel view of a fracture band in loose rock, showing a typical conjugate arrangement of the fractures. **(G)** Section of coherent rhyolite between two fracture bands. The sample is from the western slopes of Upper Sandfell. Toward the fracture bands the rhyolite becomes darker and is vesicle-poor. **(H)** Steeply inward-dipping fault north of Lower Sandfell. The fault cuts the fracture bands. Circled pen for scale. **(I)** Brecciated fault core (cataclasite) close to the southern contact with the laccolith host rock above Dal 1. The breccia consists of rounded fragments of rhyolite in a fine-grained rhyolite matrix. Pen for scale. Significant brecciation in the Sandfell laccolith is limited to a several meter-wide contact-parallel zone in the area above Dal 1.

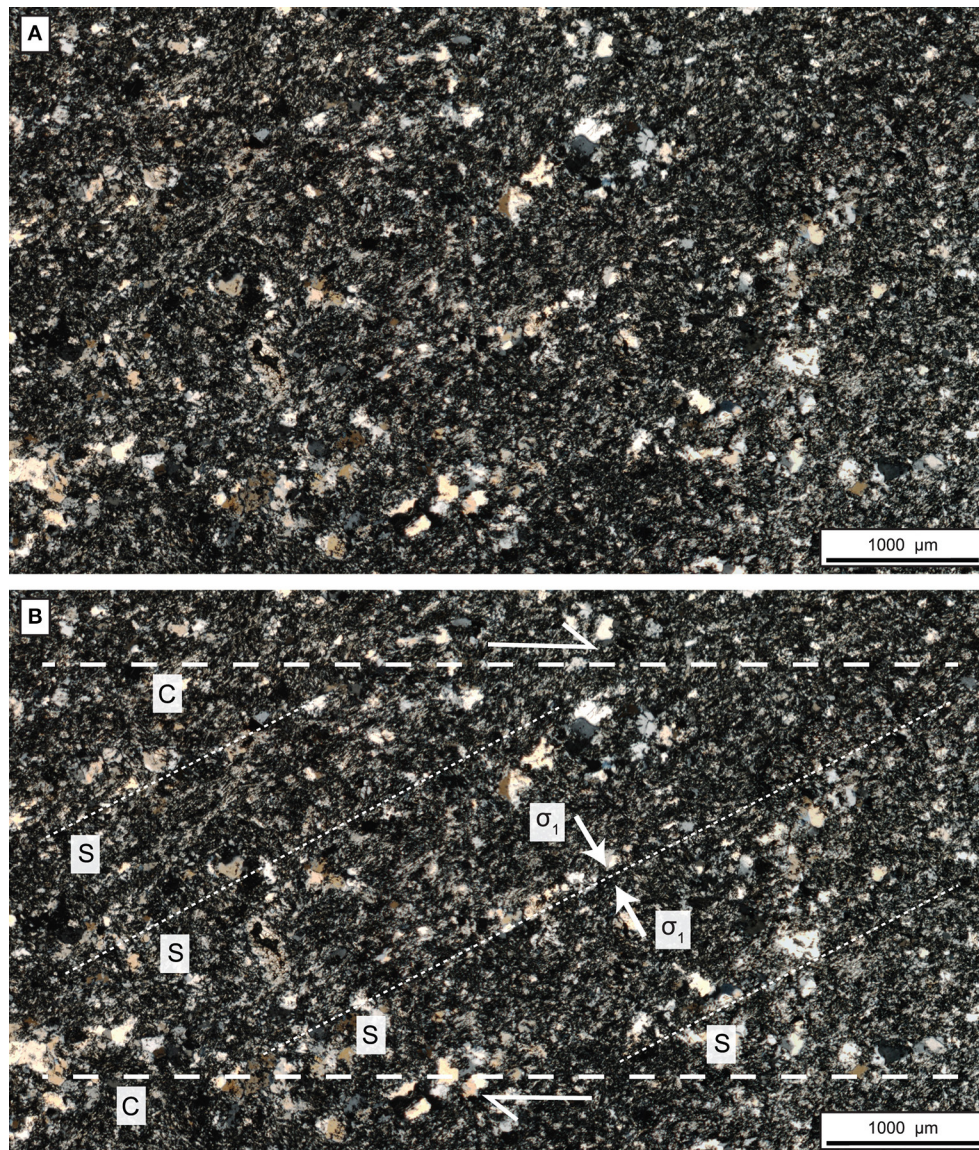
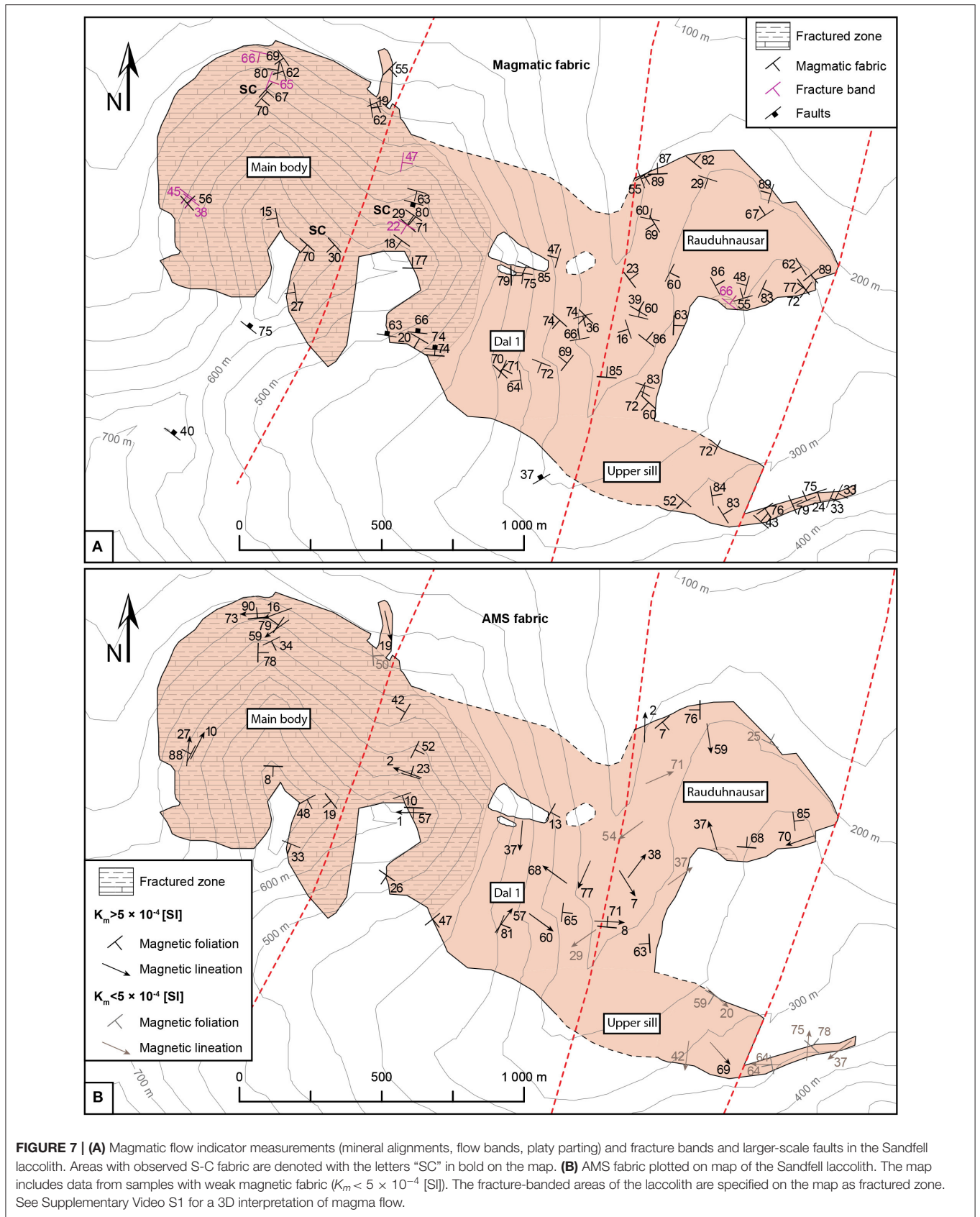


**FIGURE 6** | Unannotated **(A)** and annotated **(B)** CPL photomicrographs of the same thin section of S-C fabric in flow-banded rhyolite. The sample is from the NW part of the main body of the Sandfell laccolith. Thick dashed white lines designate C planes and thin dashed white lines S planes in **(B)**. The thin section is oriented parallel to the magnetic lineation. S-C fabrics have been identified in the studied flow-banded samples from the northern part of main body of the Sandfell laccolith (see **Figure 7A**).



are described in other felsic domes and have been used to infer the principal axes of finite strain in magma during emplacement (cf. Smith et al., 1993; Závada et al., 2009).

## Fractures and Faults in the Sandfell Laccolith

In more than one third of the Sandfell laccolith volume (0.23 km<sup>3</sup>), pervasively fractured layers occur in the rhyolite, which we call fracture bands (Figures 5C–E). Fracture bands are a consistent feature in rhyolite that crops out above 380 m a.s.l. in the main body of the laccolith, but also in a small area in southern Rauduhnausar (Figure 7). The fracture bands are cm to dm (and rarely m) thick planar features that can be followed over distances of up to hundreds of meters. The fracture bands have sharp (dike-like) tips that pinch out along strike and sometimes merge to form thicker bands (Figure 5E). Up to six fracture bands have been observed in a meter of rock, while the coherent rock in between fracture bands is sparsely fractured (Figures 5C,D). The fracture bands are generally oriented parallel to the roof and wall contacts of the laccolith (Figure 7A). For instance, in the spur north of Upper Sandfell, the geometry of the fracture bands is visibly dome-shaped. Each fracture band consist of evenly-spaced (~0.1–2 cm spacing) shear and/or tensile fractures that are orthogonal to oblique to the strike of the band. The shear fractures in the fracture bands form conjugate sets and show displacement (Figure 5F), while there is no visible displacement on the tensile fractures in the fracture bands. Rhyolite in and within 1–2 cm from a fracture band is devoid of vesicles and displays increasingly fine-grained and subhedral crystalline groundmass toward the fracture band (Figures 4E, 5G). The SLBs described in the previous section are parallel to the fractures of the fracture bands and are observed to transition into fractures between different flow bands (Figures 4C,E), which suggest that the strain-localization fabric formed contemporaneously with the fracture bands. Larger-scale faults in the main body of the laccolith cut the fracture bands (Figure 7A). Striations on polished fault-surfaces trend toward the center of the main body of the laccolith and plunge ~60°, and several of these faults have brecciated cores (Figures 5H,I).

Cooling joints are dominantly sub-vertical in the Sandfell laccolith and generally cut the fracture bands at an oblique angle (Figure 5C). The rhyolite in the fracture bands is more altered compared to the adjacent coherent rock, which indicates that the fracture bands acted as fluid pathways. The most altered samples are porous and bleached due to the alteration of the feldspar phenocrysts and groundmass into clay minerals.

## AMS Fabric

The AMS analyses of 50 block samples show that 39 of the samples have a strong to moderate bulk magnetic susceptibility (on average  $K_m = 6.3 \times 10^{-3}$  [SI], s.d.  $4.1 \times 10^{-3}$  [SI]) and 11 samples have a weak bulk magnetic susceptibility (on average  $K_m = 1.13 \times 10^{-4}$  [SI], s.d.  $8 \times 10^{-5}$  [SI]). Curie-temperature analyses indicate that magnetite is the dominant ferromagnetic mineral; however, paramagnetic minerals may also contribute to the magnetic susceptibility (cf. Butler, 1992; Supplementary Figure 1). Samples with weak bulk magnetic susceptibility are visibly altered and lack ferromagnetic minerals.

Twenty samples have a prolate magnetic fabric, 20 samples an oblate magnetic fabric, and 10 samples a triaxial magnetic fabric. The corrected degree of anisotropy ( $P_j$ ) ranges from 1.003 to 1.112 and correlates with the bulk susceptibility of the samples (Supplementary Table 1).

The magnetic foliation in the Sandfell laccolith is dominantly steeply- to moderately-dipping (88%, >35°) and parallel to the contact with the domed host rock (Figure 7B). Within the eastern part and lower part of the main body of the Sandfell laccolith, the magnetic fabric is dominantly prolate and oriented perpendicular to the contact. In the western part of the Sandfell laccolith and at higher elevations, the magnetic fabric is dominantly oblate and either parallel or oblique to the contact (Figure 8). The pole to the magnetic foliation ( $k_3$  axis) is steeply- to moderately-dipping near the flat-lying roof contacts at Upper and Lower Sandfell, while frequently sub-horizontal closer to the lateral wall contacts of the laccolith (Supplementary Figure 2).

Samples from the Upper sill are strongly altered and have a weak bulk magnetic susceptibility (Figure 7B; Supplementary Table 1). Two oxide mineral phases occur in the less altered samples: tabular magnetite phenocrysts and a second abundant fine-grained anhedral groundmass mineral phase. The tabular crystals align parallel to the mineral alignment in the samples. No evidence of multiple, temporally separated intrusions have been observed the Sandfell laccolith; secondary fabric development due to reheating is therefore unlikely (cf. Mills et al., 2011).

## Deformation and Uplift of the Host Rock

Host-rock deformation related to the emplacement of the Sandfell laccolith comprises doming, faulting, and fracturing. The “structural aureole” or host-rock dome has a maximum radius of ~900 m from the center of the laccolith, where the radius of the laccolith body is ~700 m (Figure 9). The transition from sub-horizontal to domed rock is abrupt and marked by a monocline (Figures 2C, 9). The host-rock dome is separated into rotated rock slabs bounded by normal faults at the center of the dome and reverse faults that dip toward the laccolith at the edges of the dome (Figure 9). The layering in the host-rock slab at the dome edge is almost vertical, while the layering in the host-rock slabs closer to the laccolith dips progressively less steeply. These observations show that rotation and translation along faults and minor bending enabled the doming of the host rock that accommodated the rhyolite magma (Figures 2C, 9). Similar fault geometries have been reported in cryptodome host rock in several volcanic settings worldwide (van Wyk de Vries et al., 2014).

## Results Summary

The Sandfell rhyolite displays several types of flow indicators or magmatic fabrics, including mineral alignments and flow bands that consist of varying crystal and vesicle contents and groundmass crystallinity. Magmatic and magnetic (AMS) fabrics are dominantly contact-parallel and oblate at higher elevations in the main body of the laccolith. Further away from the contact and at lower elevations in the main body of the laccolith, the magnetic fabric is dominantly prolate and perpendicular to the contact. Magmatic state conjugate SLBs overprint the flow indicators. More than one third of the volume of the Sandfell laccolith show

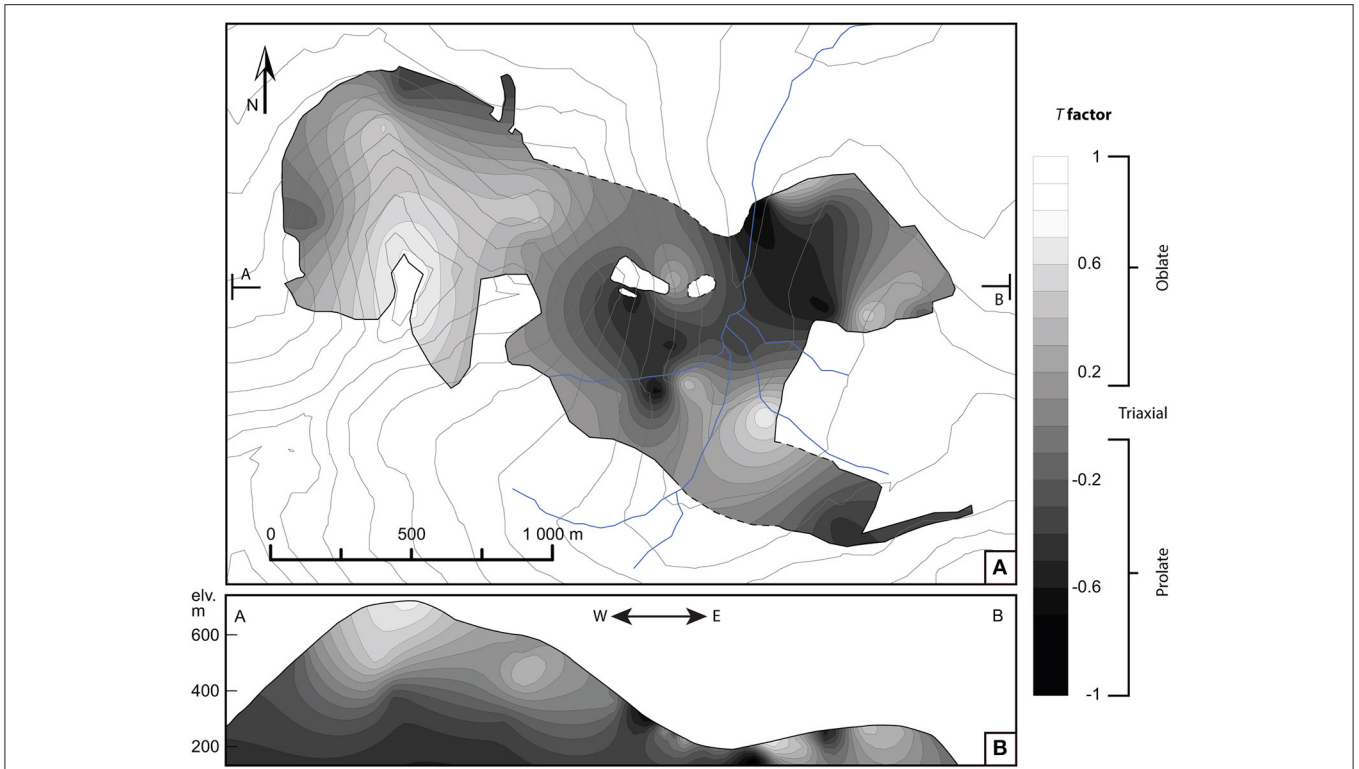


**FIGURE 8 |** Contoured map and cross-section of the shape factor  $T$  of the measured anisotropy of magnetic susceptibility in samples from across the laccolith. **(A)** In the western part of the main body of the Sandfell laccolith, the magnetic fabric is dominantly oblate, while dominantly prolate in the eastern part. See **Figure 7B** for sample locations. **(B)** Contoured cross-section of the Sandfell laccolith. The fabric shapes were contoured using elevation and easting position projected onto an E-W cross-section. The cross-section shows a correlation between magnetic fabric shape and elevation in the main body of the Sandfell laccolith.

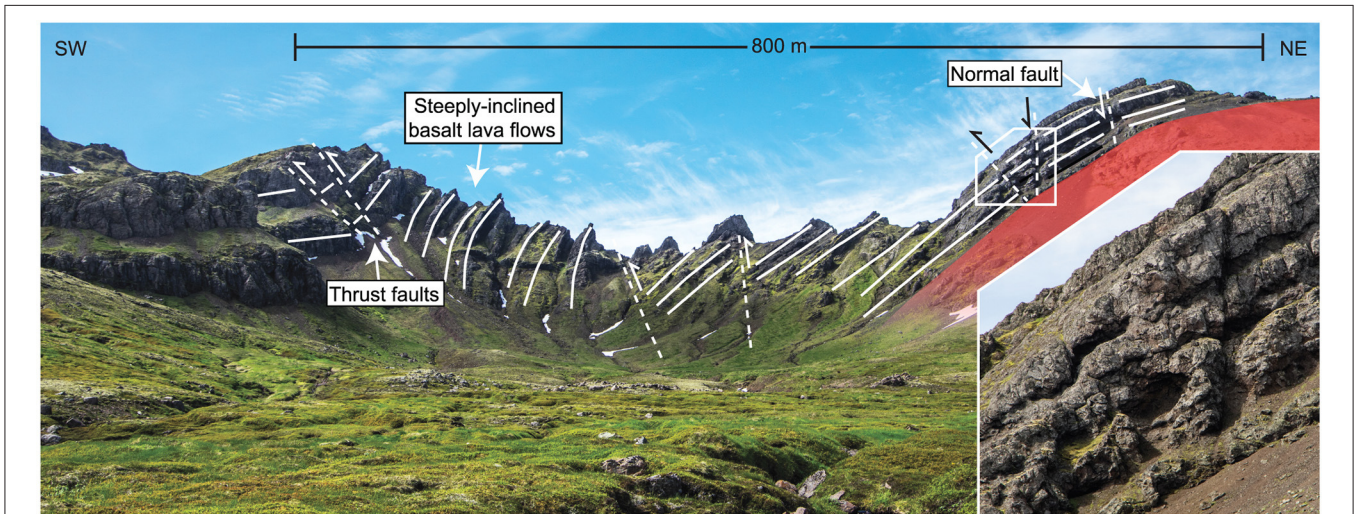


**FIGURE 9 | (A,B)** Photograph and interpretation of large-scale host-rock deformation at the south side of Upper Sandfell (compare with **Figure 2A**). The dip of the wall rock to the Sandfell laccolith changes abruptly at reverse (thrust) faults (at the edges of the host-rock dome). The roof rocks of the laccolith (the center of the host-rock dome) display normal faults (see inset in **B**). See also **Figure 2C** that shows a close up of an emplacement-related fault plane in the basalt host rock. The bulk of the rotation of the host rock that accommodated the Sandfell rhyolite magma occurred in relation to these faults.

contact-parallel intensely and systematically fractured layers. The SLBs become fracture-band fractures when transitioning between different flow bands. The rock adjacent to fractured bands is devoid of vesicles and relatively fine-grained.

## DISCUSSION

### Deciphering Magma Flow in the Sandfell Laccolith

Magma emplacement in the Sandfell laccolith can be reconstructed using a variety of structures indicative of magma flow and syn-emplacement magma deformation, including magmatic and magnetic fabrics, as well as their superposition. Generally, planar or oblate fabrics indicate flattening of magma and are oriented perpendicular to the direction of the maximum principal compressive stress ( $\sigma_1$ ) from the intruding magma. Prolate fabrics outlined by vesicle and mineral alignment, in turn, indicate stretching and shearing of the magma and form parallel to the flow direction (Paterson et al., 1998; Buisson and Merle, 2004; Závada et al., 2009).

The contact-perpendicular magmatic and magnetic fabric orientations within the Sandfell laccolith intrusion (See Dal 1 area, **Figures 7A,B**), the largely contact-parallel fabric closer to the contacts (**Figures 7A,B**), and the prolate and oblate fabric distribution within the laccolith (**Figure 8**), suggest that magma flowed from a central area under the main body of the laccolith radially outwards, and from the main body into Rauduhnausar and the Upper sill (Supplementary Video 1 for 3D interpretation of magma flow). A feeder location under the western part of the main body would explain why the bulk of the uplift in both the host rock and the laccolith is focused around Upper Sandfell, while only minor uplift occurs in the eastern part of the intrusion. The Heljara fault, under the condition that it formed before or during the emplacement of the laccolith, may have facilitated magma ascent.

The varied and sometimes complex magmatic fabric in the Sandfell laccolith is also reflected in the measured magnetic foliation, which often deviates from *in situ* measured flow banding, while the magnetic lineation ( $k_1$ ) is in good agreement (within 20° of either strike or dip azimuth) with measured flow indicators (**Figure 7**). The discrepancy in orientation between the AMS fabric and the contact-parallel flow bands in the main body of the Sandfell laccolith is most likely caused by the two crystal orientations of the S-C fabric (**Figure 6**). The dominantly oblate magnetic fabric is probably parallel to the S plane, which formed perpendicular to the maximum principal compressive stress direction ( $\sigma_1$ ) (**Figures 7, 8**), while flow bands correspond to the shear-parallel C plane. The Sandfell flow bands therefore support previous studies that show that flow bands form along shear planes and drive volatile exsolution and crystal growth as an effect of pressure drop and degassing (cf. Tuffen et al., 2003; Castro et al., 2005; Gonnermann and Manga, 2005). S-C fabric formation may also have led to compaction and porosity reduction in the magma perpendicular to the S plane, which would have increased its viscosity (cf. Ashwell et al., 2015; Kennedy et al., 2016). The orientation of the C plane parallel to

the flow banding (and the contact) suggests that the S-C fabrics in the main body of the Sandfell laccolith are induced by the combined intrusive contact-perpendicular (compressive) stresses and flexural shear due to the inflation of the magma body causing  $\sigma_1$  to be oriented 45–60° to the contact. The oblique orientation of  $\sigma_1$  promoted contact-parallel flow and indicates that flow band formation initiated at earlier stages of laccolith growth during inflation. The fine-grained and sometimes altered groundmass does, however, not permit a more detailed study of microlite orientations in the Sandfell laccolith.

### Syn-Emplacement Fracturing

The conjugate and tensile fractures in the fracture bands and the SLBs point to an orientation of  $\sigma_1$  perpendicular to the contact (and contact-parallel flow bands) during fracturing and strain localization (**Figures 4C,D**). The  $\sigma_1$  orientations together with fabric and fracture-band distribution within the laccolith suggest an internal radial push of intruding magma as the primary source of stress during fracturing (**Figures 7, 8**). The indicated maximum principal compressive stress orientations ( $\sigma_1$ ), the localized shearing in the SLBs and their relation to the layered fracturing (**Figure 4E**), strongly favor that the fracture bands formed during intrusion emplacement in the magmatic state.

The residual silicate melt of a magma has non-Newtonian properties and is susceptible to fracturing at high strain rates (Dingwell and Webb, 1989; Goto, 1999; Tuffen et al., 2003; Tuffen and Dingwell, 2005), especially when the strain rate is two orders of magnitude larger than the melt relaxation time (Dingwell, 1996; Cordonnier et al., 2012). In a magma (multi-phase fluid) with a crystal fraction <65%, the strain rate, at which the rheological transition to brittle deformation occurs, strongly depends on the viscosity of the magma, which, in turn, is controlled by temperature, crystal content and shape, bubble fraction and shape, and melt composition, including the volatile content (Dingwell, 1997; Caricchi et al., 2007; Giordano et al., 2008; Cordonnier et al., 2012; Pistone et al., 2012, 2013, 2016; Gonnermann and Manga, 2013). A non-Newtonian rheology in magma has been shown to be manifested by strain localization in the melt-phase and the onset of a strain-dependent rheology (e.g., Caricchi et al., 2007; Cordonnier et al., 2012; Pistone et al., 2016).

The occurrence of SLBs and the brittle nature of the fracture bands requires that the Sandfell magma had locally undergone a rheological transition from a magma that was able to flow (as indicated by the S-C fabric) to a viscously-stalled crystal mush that was deformed by intrusive push. Such a rheological transition of the magma from viscous flow to jamming may be related to a viscosity increase induced by crystallization and/or porosity reduction, degassing and cooling (Cashman and Blundy, 2000; Sparks et al., 2000; Giordano et al., 2008; Costa et al., 2009; Cordonnier et al., 2012; Pistone et al., 2012, 2013, 2015, 2016; Heap et al., 2015; Kennedy et al., 2016; Kushnir et al., 2017).

Anderson and Fink (1992) described vesicular bands (“striations”) in an obsidian lava flow, which they attributed to cooling, because they formed perpendicular to cooling joints. However, in the Sandfell laccolith, cooling joints are not oriented perpendicular to the fracture bands (**Figure 5C**), which indicates that fracture bands formed by another process. Even so, to test

whether cooling (conductive heat transfer) played a dominant role for increasing magma viscosity, enabling the generation the syn-emplacment strain localization and banded fracturing in the Sandfell laccolith, we modeled the cooling of a magma body with similar dimensions to the Sandfell laccolith under plausible time scales of intrusion emplacement. As the feeder of the Sandfell laccolith is not exposed, we constrain time scales of intrusion by using average extrusion rates of observed intrusive and extrusive dome building eruptions (1–10 m<sup>3</sup>/s, Newhall and Melson, 1983; Sparks et al., 1998) and estimated effusion rates of Icelandic dike-fed rhyolitic eruptions (1–10 m<sup>3</sup>/s, Höskuldsson and Sparks, 1997; Tuffen and Castro, 2009). Notably, the Cordón Caulle laccolith that was related to an ongoing eruption had a mean intrusion rate of ~300 m<sup>3</sup>/s (Castro et al., 2016). Intrusion rates of 300, 10, and 1 m<sup>3</sup>/s would fill the 0.57 km<sup>3</sup> Sandfell laccolith in about 22 days, 22 months, and 18 years, respectively. However, since the Sandfell laccolith was not associated with an extensive explosive eruption, an intrusion rate in the lower range of the spectrum is more likely (cf. Mastin, 2002).

The temperature distribution within the modeled magma body and the host rock are calculated using an FEM model, by solving for the pure conductive heat transfer (Equation 4).

$$\rho C_p \frac{\partial T}{\partial t} + \nabla(-k\nabla T) = 0 \quad (4)$$

Where the equation parameters are density ( $\rho$ ), specific heat at constant pressure ( $C_p$ ), temperature ( $T$ ), time ( $t$ ), and thermal conductivity ( $k$ ) (see **Table 1** for input values). We assume the effects of viscous heating and pressure-volume work to be negligible. The modeled magma reservoir is considered to be completely liquid and emplaced in a single episode, immediately before it starts to cool. Since the cooling model is static, it does not take into account cooling during inflation, and the cooling time is an upper limit as it cools by conduction. Groundwater circulation or latent heat of crystallization are also not considered in the model. The Sandfell rhyolite groundmass is crystalline, which suggests that the magma solidified by crystallization. When a rhyolite magma contains >65% solid phases (crystals), it reaches the point of “lock-up” of the crystal mush, where the crystals become the controlling factor of the rheology, which could lead to brittle deformation if the crystal mush is stressed at sufficient strain rates (Marsh, 1981; Petford, 2003; Caricchi et al., 2007; Lavallée et al., 2007; Cordonnier et al., 2012; Pistone et al., 2017). We therefore assume that the rhyolite magma is able to fracture with an associated strain rate due to non-Newtonian

behavior, when >65% of the magma body has crystallized. The temperature, at which the modeled Sandfell rhyolite magma contains >65% solids, is estimated to ~820°C (1093.15 K) for a confining pressure of 30 MPa, using the whole-rock composition of the Sandfell rhyolite from Martin and Sigmarsson (2010) and Rhyolite MELTS v. 1.1 with equilibration crystallization (Ghiorso and Sack, 1995; Gualda et al., 2012; Ghiorso and Gualda, 2015).

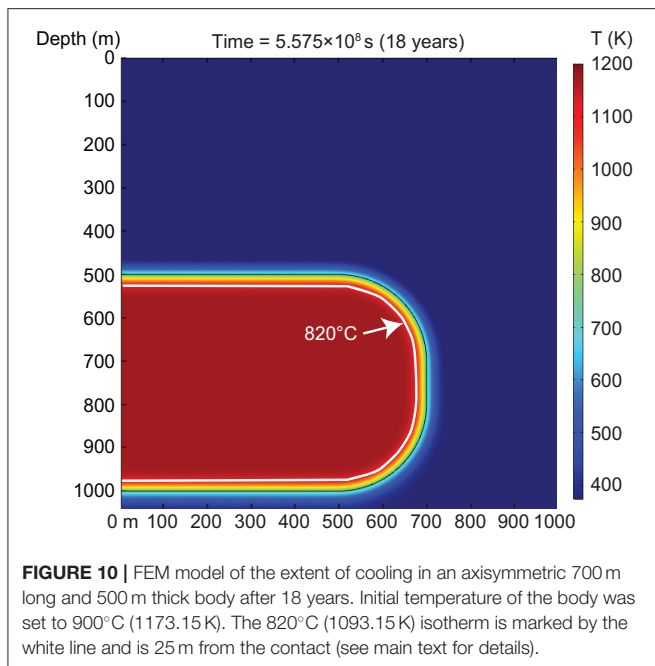
In the modeled magma body, a 1.5, 8, 25 m thick rim cooled below 820°C (1093.15 K), after 22 days, 22 months, 18 years of cooling by conductive heat transfer, respectively (**Figure 10**). Since the thickness of fracture banded area in the main body of the Sandfell laccolith is at least 200 m, our cooling model demonstrates that pure conductive heat transfer is not able to account for the generation of fracture bands or the viscosity increase of the rhyolite magma in the estimated intrusion time scales.

Another potential cause for the viscous stalling of the Sandfell rhyolite is strain-induced degassing (cf. Sparks et al., 2000; Cordonnier et al., 2012; Pistone et al., 2012, 2013, 2015, 2016; Galetto et al., 2017; Kushnir et al., 2017). Transport of the Sandfell rhyolite magma from a deeper source to the emplacement location most likely entailed a pressure change. We assume that the rhyolite magma was transported at moderate to slow ascent rates, since the intrusive event was not accompanied by extensive extrusive activity (cf. Hawkes and Hawkes, 1933; Gibson et al., 1966; Mastin, 2002). A moderate to slow ascent of the Sandfell rhyolite would have promoted oversaturation inducing some bubble formation and crystallization that increased the viscosity of the magma (cf. Westrich et al., 1988; Swanson et al., 1989; Cashman and Blundy, 2000; Gonnermann and Manga, 2007). The low vesicle content in coherent fracture-poor rhyolite exposed in the lower parts of Sandfell and the overall small vesicle sizes in fractured rock suggest that the Sandfell rhyolite was quite impermeable and therefore could not have effectively been degassing due to the transport from source to emplacement location (**Figure 5G**). However, Ashwell et al. (2015) showed in experiments on rhyolitic dome lavas that the porosity of the lava decreased at a constant shear rate. Reducing the porosity in magma by compaction, pore collapse and/or degassing increases the magma viscosity (Ashwell et al., 2015; Heap et al., 2015; Kushnir et al., 2017). This implies that the intruding magma could have compacted the already emplaced magma and reduced the porosity over time, making the Sandfell rhyolite progressively more viscous (cf. Kennedy et al., 2016).

The vesicle-poor rock and the diffusely microcrystalline groundmass in and next to the fracture bands, point to that

**TABLE 1** | Thermal properties used for cooling model.

| Property                                               | Host rock | Liquid | References                                           |
|--------------------------------------------------------|-----------|--------|------------------------------------------------------|
| Thermal conductivity ( $k$ ) (W/(m °C))                | 1.48      | 1.5    | Leshner and Spera, 2015                              |
| Heat capacity at constant pressure ( $C_p$ ) (J/kg °C) | 1,230     | 1,604  | Turcotte and Schubert, 2002; Leshner and Spera, 2015 |
| Initial temperature (T) (°C)                           |           | 900    | Höskuldsson and Sparks, 1997                         |
| Density ( $\rho$ ) (kg/m <sup>3</sup> )                | 2,700     | 2,300  | Höskuldsson and Sparks, 1997                         |
| Geothermal gradient (°C/km)                            | 100       |        | Flóvenz and Saemundsson, 1993                        |



degassing and/or porosity reduction in the Sandfell rhyolite were primarily facilitated by the fracture bands forming, which increased the permeability in the magma and led to rapid crystallization due to undercooling (Hammer and Rutherford, 2002; Cabrera et al., 2011; Castro et al., 2012; Pistone et al., 2013; Shields et al., 2014; Heap and Kennedy, 2016; Kushnir et al., 2017). Several studies have shown that strain localization and fracturing induces local decompression, which causes volatiles to degas/escape along the strain planes (Okumura et al., 2009, 2010; Caricchi et al., 2011; Castro et al., 2012; Kushnir et al., 2017). Castro et al. (2012) estimated the degassing time scales for a 0.2 wt.% decrease of H<sub>2</sub>O through 0.1–1 cm spaced fractured melt to range from  $\sim 10^5$  to  $10^7$  s, respectively. Microlite growth rates for a decompressing silicic magma have been experimentally determined to  $\sim 1.0 \times 10^{-6}$  mm/s (Hammer and Rutherford, 2002), which would crystallize the microlites in the Sandfell rhyolite groundmass in <14 h. These time scales display that fracture-band degassing could have been contemporaneous with groundmass crystallization. The crystallinity in the Sandfell rhyolite before the onset of fracture-band formation could therefore have been more or less similar to the phenocryst content (crystal fraction  $\sim 6\%$ , but up to 30% in flow bands). The widespread occurrence of fracture bands in the Sandfell laccolith therefore indicates that fracture-band formation created a highly permeable network of fractures that efficiently enhanced degassing potential of the magma and caused rapid increase in viscosity and solidification of the Sandfell rhyolite. There are no degassing-induced fractures such as tuffites observed in the host rock to the Sandfell laccolith (cf. Stasiuk et al., 1996), although degassing could have been facilitated by the pre-existing cooling joints and the emplacement-related faults in the host rock (Figure 9). Moreover, fragmented remnants of pore collapse are not observed in the Sandfell rhyolite and vesicles

are generally small and rounded, which suggests that porosity reduction during the onset of fracturing was probably achieved by volatiles leaving the magma via the densely-spaced fractures (cf. Kushnir et al., 2017) as opposed to porosity reduction by compaction of the magma (cf. Heap et al., 2015; Kennedy et al., 2016).

The fractures (both tensile and shear) in the fracture bands and the SLBs in the Sandfell rhyolite indicate a shear thickening rheology during fracture-band formation, which is consistent with experimental data that display viscosity increase with increasing strain rates in crystal-poor magmas (Pistone et al., 2016). Shear thickening or dilatant behavior of the magma also favors degassing by increasing the permeability of the magma (Nara et al., 2011; Shields et al., 2014; Heap et al., 2015; Heap and Kennedy, 2016; Kushnir et al., 2017). The transitions from SLBs to fractures between different flow bands show that the Sandfell magma contemporaneously deformed in a brittle and a ductile “magmatic” fashion in adjacent areas (Figure 4E). This further demonstrates that viscous stalling must have been contemporary with fracturing and that the banded distribution of the fractures is related to the flow bands. Differences in bubble and crystal fraction between the different flow bands in the Sandfell rhyolite would yield differences in viscosity (cf. Caricchi et al., 2007; Cordonnier et al., 2012; Shields et al., 2014). Additionally, Wright and Weinberg (2009) showed that bubbles in a magma promote strain localization. The heterogeneous crystal and vesicle fractions of the flow bands in the Sandfell laccolith could therefore have induced a different rheological response to the localized stress (cf. Smith et al., 2001; Cordonnier et al., 2012; Shields et al., 2014; Ashwell et al., 2015; Pistone et al., 2017). Once initiated, the fracture bands also propagated as suggested by the dyke-like tips of the bands (Figure 5E). Propagation occurred in a plane perpendicular to the maximum principal compressive stress direction, which is indicated by the acute angle of the conjugate fractures in the fracture bands (Figures 4C,D, 5F, 11). Simultaneously, the fracture bands grew thicker beyond the constraints of the flow banding by propagation of the individual fractures, as demonstrated by fracture bands merging.

The rheological evolution of the Sandfell rhyolite can be summarized as follows: Initial viscosity increase in the Sandfell rhyolite magma can be attributed to volatile exsolution and crystallization due to transport of magma at moderate to slow ascent rates from the source of the magma to its emplacement location (cf. Cashman and Blundy, 2000), flow fabric formation (cf. Castro et al., 2005; Gonnermann and Manga, 2005) and compaction (cf. Ashwell et al., 2015; Heap et al., 2015; Kennedy et al., 2016). This viscosity increase led to a non-Newtonian behavior of the magma in response to intrusive stress. Decompression related to strain localization and fracturing in the magma caused volatiles to exsolve and escape along the strain planes, which is supported by microstructures and textures in the Sandfell rhyolite (cf. Tuffen et al., 2003; Caricchi et al., 2011; Castro et al., 2012; Pistone et al., 2013; Kushnir et al., 2017). The fracture-induced degassing promoted porosity reduction and rapid crystallization in the magma due to undercooling, which increased the magma viscosity and solidified the magma locally (cf. Westrich et al., 1988; Cashman and Blundy, 2000;

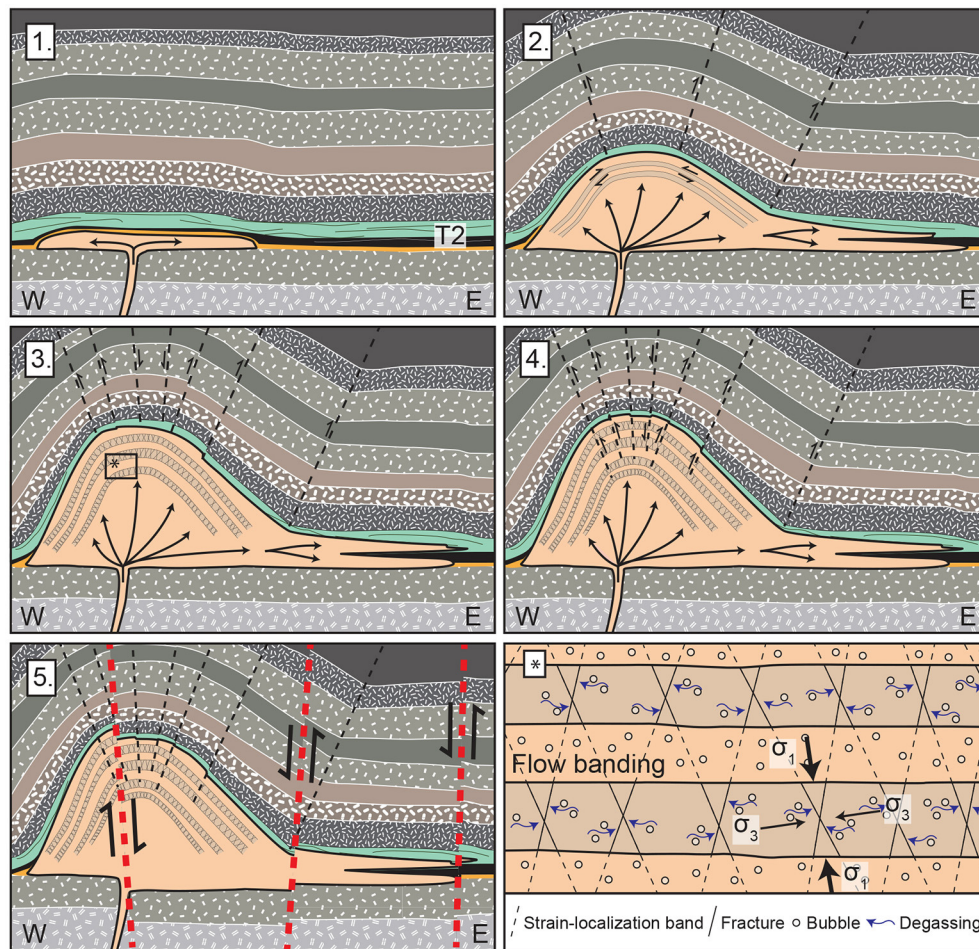


**FIGURE 11** | (1) The formation of the Sandfell laccolith initiated as a sill intrusion (cf. Johnson and Pollard, 1973). (2) The sill started to inflate into a laccolith. Distinct flow banding formed by contact-parallel flow driven by push from intruding magma and shear due to magma body inflation. Two lobes of the rhyolite magma intruded at different stratigraphic levels of T2 to the east, forming Rauduhnausar and the Upper sill. (3) The inflation of the magma body continued, while the eastern lobes only marginally inflated. Viscosity increase in the magma was promoted by crystallization related to the flow banding and porosity reduction and compaction of the magma by the intrusive stress from continuously intruding magma (cf. Ashwell et al., 2015). During later stages of emplacement strain-localization fabrics developed in the magma (\*). When subject to localized shearing, flow bands in the magma responded differently—some flow bands deformed in a brittle fashion and fractured, while other parts of the magma developed SLBs. Volatile exsolution and escape from the magma body where facilitated by decompression induced by fracture-band formation. This rapidly increased the viscosity of the magma aided by crystallization and porosity reduction and essentially solidified the rim of the laccolith. The tilted acute bisector planes of the conjugate fractures bands are probably attributed to minor shear during and after fracture-band formation. (4) The solidified part of the Sandfell laccolith was faulted and deformed by the still intruding magma in a similar fashion as the host rock, as evident by internal larger-scale faults, dipping toward the center of the laccolith. (5) Regional faults created a graben in the central part of the laccolith. Some of the regional faulting may have occurred prior to and during emplacement of the Sandfell laccolith (see Supplementary Information 2).

Sparks et al., 2000; Hammer and Rutherford, 2002; Castro et al., 2012; Pistone et al., 2013; Kushnir et al., 2017). Additionally, the degassing was probably aided by weakening of the host through the large-scale faulting of host rock (Figures 2C, 3D, 9). The uplift and displacement of the host rock along the faults (punching) brought the magma closer to the surface, while increasing the stress on the non-Newtonian magma in the rim of the intrusion (Figures 9, 11). We propose that intrusive push built up stresses at the degassing-induced “solidification” front in the magma body, which were released in pulses by the formation of fracture bands. Hence, fracturing in the flow bands migrated toward the center of the laccolith as it inflated (Figure 11).

## Emplacement of the Sandfell Laccolith

Since the Sandfell laccolith formed during a single intrusive event and fracture bands occur in more than one third of its volume, strain localization and fracturing solidified the rim of the laccolith body and transformed the earlier-intruded magma to a brittle host of the subsequently intruding magma, during emplacement. Concentric syn-emplacement fracturing and auto-brecciation are recorded in solidified and exposed cryptodomes emplaced into both water-saturated sediments and into sub-aerial volcanic edifices (Snyder and Fraser, 1963; Goto and McPhie, 1998; Goto et al., 2000, 2004; Stewart and McPhie, 2003). This suggests that strain-induced fracturing and degassing are an important process for regulating magma behavior in cryptodomes worldwide, as is

observed in volcanic conduits (cf. Sparks et al., 2000; Kendrick et al., 2016).

Moreover, if the host rock exerted the dominant control on intrusion emplacement, most of the deformation should be accommodated in the host rock (Pollard and Johnson, 1973; Jackson and Pollard, 1988; Kerr and Pollard, 1998; Bunger and Cruden, 2011). However, extensive fracturing and faulting occurred within the Sandfell laccolith despite the fault-aided doming of the host rock. For example, the inward-dipping faults in the fractured rim of the Sandfell laccolith are similar to the thrust faults in the host-rock dome (**Figures 2H,I, 7A, 9, 11**), which demonstrates that the solidified part of the laccolith deformed in a similar way to the host rock. This implies that the host-rock properties became less important after the initial stage of the emplacement of the Sandfell laccolith, because the highly viscous fractured rim of the intrusion successively took over as host to the less viscous intruding magma. Furthermore, by solidifying the rim of the intrusion, magma flow likely focused centrally within the body and amplified the dome-shape (cf. Currier and Marsh, 2015). Interestingly, the extent of syn-emplacement degassing and solidification observed in the Sandfell laccolith would lead to a pressure drop due to the loss of volatiles from the magma (cf. John and Blundy, 1993; Marsh, 1996; Žák et al., 2009), which might have induced a pressure gradient that drove new magma into the intrusion. Our observations show that extensive solidification is an important factor during time scales of emplacement of viscous magma intrusions in the uppermost kilometer of the crust, and that rheological changes in intruding magma may affect the mechanism of emplacement and the growth of the intrusion.

## Implications for Volcanic Hazards during Cryptodome Emplacement

In the Sandfell laccolith, the rapid syn-emplacement solidification would have limited the amount of eruptible magma and so decreased the likelihood of an eruption. This is supported by the small volume of the Sandfell tuff (Hawkes and Hawkes, 1933), which shows that only minor extrusive activity, if any, occurred during the intrusion. At the same time, internal faulting, as observed in the Sandfell laccolith, could reduce the stability of the magma body and create potential weakness planes that promote edifice collapse (Donnadieu et al., 2001; Merle and Lénat, 2003; Oehler et al., 2005). Furthermore, since no hydrothermal system is observed in the host rock of the Sandfell laccolith, the alteration observed in fracture bands might be induced by escaping fluids from the degassing magma. If Sandfell-type processes occur in other cryptodomes, it may potentially weaken the solidified part of the magma body along fracture and fault planes and increase the risk for collapse (cf. van Wyk de Vries et al., 2000).

## CONCLUSIONS

The Sandfell laccolith intruded at about 500 m depth into the Neogene lava pile in Iceland and can therefore be considered a cryptodome. Magmatic and magnetic fabrics show that the magma flowed in a single intrusive event from a

central area beneath the main dome-shaped body toward and parallel to the contacts. Microstructural analyses of the Sandfell laccolith indicate that during emplacement, the rhyolite magma underwent a rheological transition from a flowing magma to a stalled viscous crystal mush that became the host of the subsequently emplaced magma. We suggest that viscous stalling was a result of compaction by intrusive stresses and rapid crystallization caused by a pressure drop due to strain localization and fracturing in the magma, which resulted in distinctive fracture-rich layers in more than one third of the volume of the laccolith. The outer rim of the Sandfell laccolith essentially solidified during intrusion emplacement and was deformed in a similar fashion to the host rock. The deformation processes that occur in the magma during the emplacement of viscous magma bodies in the uppermost kilometer of the crust, can therefore exert control on the shape of the intrusion and limit the amount of eruptible magma.

## AUTHOR CONTRIBUTIONS

SB: Initiated the project; TM and SB: Conducted field work and collected the samples; BA: Facilitated the AMS analysis; TM: Carried out the analytical work and ER made the cooling models; The manuscript was written by TM and SB with input from all authors.

## FUNDING

Field work was funded by Uddeholms travel stipend (Värmlands nation, Uppsala, Sweden), Otterborgs travel stipend and the Swedish Royal Academy of Science (KVA). The research was funded by the Swedish Research Council (VR) grant 2015-03931\_VR. ER is funded by the Center of Natural Hazards and Disaster Science (CNDS).

## ACKNOWLEDGMENTS

We thank the G. P. L. Walker museum Breiðdalssetur in Breiðdalsvík, eastern Iceland for providing unpublished maps and doctoral dissertations on the area. We thank the Swedish Geological Survey (SGU) for access to their core-drilling facilities and Adam Bohlin for help with sample preparation and AMS analyses. The study benefitted from discussions with Mohsen Bazargan, Olivier Galland, Olafur Gudmundsson, Christoph Hieronymous, Valentin Troll, Hugh Tuffen, Rémi Vachon, and the participants of the Nordvulk summer school on magmatic plumbing systems. We thank Mattia Pistone for comments that greatly improved the manuscript. We thank Ben Kennedy and Alessandro Tibaldi for their reviews and editors Shanaka De Silva and Valerio Acocella for comments that improved the manuscript. An academic license for Midland Valley Ltd. MOVE<sup>TM</sup> software package is gratefully acknowledged.

## SUPPLEMENTARY MATERIAL

The Supplementary Material for this article can be found online at: <https://www.frontiersin.org/articles/10.3389/feart.2018.00005/full#supplementary-material>

## REFERENCES

- Anderson, S. W., and Fink, J. H. (1992). Crease structures: indicators of emplacement rates and surface stress regimes of lava flows. *Geol. Soc. Am. Bull.* 104, 615–625. doi: 10.1130/0016-7606(1992)104<0615:CSIOER>2.3.CO;2
- Ashwell, P. A., Kendrick, J. E., Lavallée, Y., Kennedy, B. M., Hess, K.-U., von Aulock, F. W., et al. (2015). Permeability of compacting porous lavas. *J. Geophys. Res. Solid Earth* 120, 1605–1622. doi: 10.1002/2014JB011519
- Benn, K., and Allard, B. (1989). Preferred mineral orientations related to magmatic flow in ophiolite layered gabbros. *J. Petrol.* 30, 925–946. doi: 10.1093/ptetrology/30.4.925
- Borradaile, G. J., and Jackson, M. (2010). Structural geology, petrofabrics and magnetic fabrics (AMS, AARM, AIRM). *J. Struct. Geol.* 32, 1519–1551. doi: 10.1016/j.jsg.2009.09.006
- Brothers, R. N. (1964). Petrofabric analyses of Rhum and Skaergaard layered rocks. *J. Petrol.* 5, 255–274. doi: 10.1093/ptetrology/5.2.255
- Buisson, C., and Merle, O. (2004). Numerical simulation of strain within lava domes. *J. Struct. Geol.* 26, 847–853. doi: 10.1016/j.jsg.2003.11.017
- Bunger, A. P., and Cruden, A. R. (2011). Modeling the growth of laccoliths and large mafic sills: role of magma body forces. *J. Geophys. Res.* 116:B02203. doi: 10.1029/2010JB007648
- Butler, R. F. (1992). *PALEOMAGNETISM: Magnetic Domains to Geologic Terranes*. Boston: Blackwell Scientific, 237.
- Cabrera, A., Weinberg, R. F., Wright, H. M. N., Zlotnik, S., and Cas, R. A. F. (2011). Melt fracturing and healing: a mechanism for degassing and origin of silicic obsidian. *Geology* 39, 67–70. doi: 10.1130/G31355.1
- Cañón-Tapia, E., and Herrero-Bervera, E. (2009). Sampling strategies and the anisotropy of magnetic susceptibility of dykes. *Tectonophysics* 466, 3–17. doi: 10.1016/j.tecto.2008.11.012
- Caricchi, L., Burlini, L., Ulmer, P., Gerya, T., Vassalli, M., and Papale, P. (2007). Non-Newtonian rheology of crystal-bearing magmas and implications for magma ascent dynamics. *Earth Planet. Sci. Lett.* 264, 402–419. doi: 10.1016/j.epsl.2007.09.032
- Caricchi, L., Pommier, A., Pistone, M., Castro, J., Burgisser, A., and Perugini, D. (2011). Strain-induced magma degassing: insights from simple-shear experiments on bubble bearing melts. *Bull. Volcanol.* 73, 1245–1257. doi: 10.1007/s00445-011-0471-2
- Cashman, K., and Blundy, J. (2000). Degassing and crystallization of ascending andesite and dacite. *Philos. Trans. R. Soc. A Math. Phys. Eng. Sci.* 358, 1487–1513. doi: 10.1098/rsta.2000.0600
- Castro, J. M., Cordonnier, B., Schipper, C. I., Tuffen, H., Baumann, T. S., and Feisel, Y. (2016). Rapid laccolith intrusion driven by explosive volcanic eruption. *Nat. Commun.* 7:13585. doi: 10.1038/ncomms13585
- Castro, J. M., Cordonnier, B., Tuffen, H., Tobin, M. J., Puskar, L., Martin, M. C., et al. (2012). The role of melt-fracture degassing in defusing explosive rhyolite eruptions at volcán Chaitén. *Earth Planet. Sci. Lett.* 333–334, 63–69. doi: 10.1016/j.epsl.2012.04.024
- Castro, J. M., Dingwell, D. B., Nichols, A. R. L., and Gardner, J. E. (2005). “New insights on the origin of flow bands in obsidian,” in *Special Paper 396: Kinematics and dynamics of lava flows*, eds M. Manga and G. Ventura (Boulder, CO: Geological Society of America), 55–65. doi: 10.1130/0-8137-2396-5.55
- Cordonnier, B., Caricchi, L., Pistone, M., Castro, J., Hess, K.-U., Gottschaller, S., et al. (2012). The viscous-brittle transition of crystal-bearing silicic melt: direct observation of magma rupture and healing. *Geology* 40, 611–614. doi: 10.1130/G3914.1
- Corry, C. E. (1988). Laccoliths; mechanics of emplacement and growth. *GSA Spec. Pap.* 220, 1–114. doi: 10.1130/SPE220-p1
- Costa, A., Caricchi, L., and Bagdassarov, N. (2009). A model for the rheology of particle-bearing suspensions and partially molten rocks. *Geochem. Geophys. Geosyst.* 10:Q03010. doi: 10.1029/2008GC002138
- Currier, R. M., and Marsh, B. D. (2015). Mapping real time growth of experimental laccoliths: the effect of solidification on the mechanics of magmatic intrusion. *J. Volcanol. Geotherm. Res.* 302, 211–224. doi: 10.1016/j.jvolgeores.2015.07.009
- de Jesus Padilla, A. (2015). *Elemental and Isotopic Geochemistry of Crystal-Melt Systems: Elucidating the Construction and Evolution of Silicic Magmas in the Shallow Crust, using Examples from Southeast Iceland and Southwest USA*. Ph.D. Dissertation, Vanderbilt University, Nashville, TN, 288.
- de Saint-Blanquat, M., Habert, G., Horsman, E., Morgan, S. S., Tikoff, B., Launeau, P., et al. (2006). Mechanisms and duration of non-tectonically assisted magma emplacement in the upper crust: the Black Mesa pluton, Henry mountains, Utah. *Tectonophysics* 428, 1–31. doi: 10.1016/j.tecto.2006.07.014
- Dingwell, D. B. (1996). Volcanic dilemma—flow or blow? *Science* 273, 1054–1055.
- Dingwell, D. B. (1997). The brittle-ductile transition in high-level granitic magmas: material constraints. *J. Petrol.* 38, 1635–1644. doi: 10.1093/ptetroj/38.12.1635
- Dingwell, D. B., and Webb, S. L. (1989). Structural relaxation in silicate melts and non-Newtonian melt rheology in geologic processes. *Phys. Chem. Miner.* 16, 508–516. doi: 10.1007/BF00197020
- Donnadieu, F., Merle, O., and Besson, J.-C. (2001). Volcanic edifice stability during cryptodome intrusion. *Bull. Volcanol.* 63, 61–72. doi: 10.1007/s004450000122
- Eriksson, P. I., Riisshuus, M. S., Sigmundsson, F., and Elming, S.-Å. (2011). Magma flow directions inferred from field evidence and magnetic fabric studies of the Streitishvarf composite dike in east Iceland. *J. Volcanol. Geotherm. Res.* 206, 30–45. doi: 10.1016/j.jvolgeores.2011.05.009
- Flóvenz, Ó. G., and Saemundsson, K. (1993). Heat flow and geothermal processes in Iceland. *Tectonophysics* 225, 123–138. doi: 10.1016/0040-1951(93)90253-G
- Galetto, F., Acocella, V., and Caricchi, L. (2017). Caldera resurgence driven by magma viscosity contrasts. *Nat. Commun.* 8:1750. doi: 10.1038/s41467-017-01632-y
- Geoffroy, L., Callot, J. P., Aubourg, C., and Moreira, M. (2002). Magnetic and plagioclase linear fabric discrepancy in dykes: a new way to define the flow vector using magnetic foliation. *Terra Nov.* 14, 183–190. doi: 10.1046/j.1365-3121.2002.00412.x
- Ghiorso, M. S., and Gualda, G. A. R. (2015). An H<sub>2</sub>O–CO<sub>2</sub> mixed fluid saturation model compatible with rhyolite-MELTS. *Contrib. Mineral. Petrol.* 169:53. doi: 10.1007/s00410-015-1141-8
- Ghiorso, M. S., and Sack, R. O. (1995). Chemical mass transfer in magmatic processes IV. A revised and internally consistent thermodynamic model for the interpolation and extrapolation of liquid-solid equilibria in magmatic systems at elevated temperatures and pressures. *Contrib. Mineral. Petrol.* 119, 197–212. doi: 10.1007/BF00307281
- Gibson, I. L. (1963). *The Reydarfjörður Acid Volcano Centre of Eastern Iceland*. Ph.D. dissertation, Imperial College, University of London, London, 267.
- Gibson, I. L., Kinsman, D. J. J., and Walker, G. P. L. (1966). *Geology of the Fáskrúðsfjörður Area, Eastern Iceland*. Reykjavík: Vísindafélag Íslandinga, 1–52.
- Gilbert, G. K. (1877). *Report on the Geology of the Henry Mountains*. US Geographical and Geological Survey, Washington, DC.
- Giordano, D., Russell, J. K., and Dingwell, D. B. (2008). Viscosity of magmatic liquids: a model. *Earth Planet. Sci. Lett.* 271, 123–134. doi: 10.1016/j.epsl.2008.03.038
- Gonnermann, H. M., and Manga, M. (2003). Explosive volcanism may not be an inevitable consequence of magma fragmentation. *Nature* 426, 432–435. doi: 10.1038/nature02138
- Gonnermann, H. M., and Manga, M. (2005). Flow banding in obsidian: a record of evolving textural heterogeneity during magma deformation. *Earth Planet. Sci. Lett.* 236, 135–147. doi: 10.1016/j.epsl.2005.04.031
- Gonnermann, H. M., and Manga, M. (2007). The fluid mechanics inside a volcano. *Annu. Rev. Fluid Mech.* 39, 321–356. doi: 10.1146/annurev.fluid.39.050905.110207
- Gonnermann, H. M., and Manga, M. (2013). “Dynamics of magma ascent in the volcanic conduit,” in *Modeling Volcanic Processes*, eds S. A. Fagents, T. K. P. Gregg, and R. M. C. Lopes (Cambridge: Cambridge University Press), 55–84.
- Goto, A. (1999). A new model for volcanic earthquake at Unzen volcano: melt rupture model. *Geophys. Res. Lett.* 26, 2541–2544. doi: 10.1029/1999GL900569
- Goto, Y., and McPhie, J. (1998). Endogenous growth of a Miocene submarine dacite cryptodome, Rebun Island, Hokkaido, Japan. *J. Volcanol. Geotherm. Res.* 84, 273–286. doi: 10.1016/S0377-0273(98)00040-7
- Goto, Y., Ito, Y., Yokoyama, Y., Matsui, T., and Mimatsu, S. (2004). Internal structures of a subaerial dacite cryptodome at Usu volcano, Hokkaido, Japan. *Mem. Muroan Inst. Tech.* 54, 3–10.
- Goto, Y., Shingo, K., Noriyoshi, T., and Katsuto, N. (2000). “Internal structures and fracture networks in a Miocene Dacite Intrusion, Rebun Island, Hokkaido, Japan,” in World Geothermal Congress (International Geothermal Association), R0144.

- Gualda, G. A. R., Ghiorso, M. S., Lemons, R. V., and Carley, T. L. (2012). Rhyolite-MELTS: a Modified Calibration of MELTS optimized for Silica-rich, fluid-bearing magmatic systems. *J. Petrol.* 53, 875–890. doi: 10.1093/ptrology/egr080
- Hammer, J. E., and Rutherford, M. J. (2002). An experimental study of the kinetics of decompression-induced crystallization in silicic melt. *J. Geophys. Res. Solid Earth* 107, ECV 8-1–ECV 8-24. doi: 10.1029/2001JB000281
- Hawkes, L., and Hawkes, H. K. (1933). The Sandfell Laccolith and “Dome of Elevation.” *Q. J. Geol. Soc.* 89, 379–400.
- Heap, M. J., and Kennedy, B. M. (2016). Exploring the scale-dependent permeability of fractured andesite. *Earth Planet. Sci. Lett.* 447, 139–150. doi: 10.1016/j.epsl.2016.05.004
- Heap, M. J., Kennedy, B. M., Pernin, N., Jacquemard, L., Baud, P., Farquharson, J. I., et al. (2015). Mechanical behaviour and failure modes in the Whakaari (White Island volcano) hydrothermal system, New Zealand. *J. Volcanol. Geotherm. Res.* 295, 26–42. doi: 10.1016/j.jvolgeores.2015.02.012
- Holness, M. B., Sides, R., Prior, D. J., Cheadle, M. J., and Upton, B. G. J. (2012). The peridotite plugs of Rum: Crystal settling and fabric development in magma conduits. *Lithos* 134–135, 23–40. doi: 10.1016/j.lithos.2011.11.024
- Horsman, E., Morgan, S., de Saint-Blanquat, M., Habert, G., Nugent, A., Hunter, R. A., et al. (2009). Emplacement and assembly of shallow intrusions from multiple magma pulses, Henry Mountains, Utah. *Earth Environ. Sci. Trans. R. Soc. Edinburgh* 100, 117–132. doi: 10.1017/S1755691009016089
- Höskuldsson, A., and Sparks, R. S. J. (1997). Thermodynamics and fluid dynamics of effusive subglacial eruptions. *Bull. Volcanol.* 59, 219–230. doi: 10.1007/s004450050187
- Hrouda, F., and Ježek, J. (1999). Theoretical models for the relationship between magnetic anisotropy and strain: effect of triaxial magnetic grains. *Tectonophysics* 301, 183–190. doi: 10.1016/S0040-1951(98)00267-4
- Jackson, M. D., and Pollard, D. D. (1988). The laccolith-stock controversy: new results from the southern Henry Mountains, Utah. *Geol. Soc. Am. Bull.* 100, 117–139. doi: 10.1130/0016-7606(1988)100<117:TLSCNR>&t.3.CO;2
- Jelinek, V. (1981). Characterization of the magnetic fabric of rocks. *Tectonophysics* 79, T63–T67. doi: 10.1016/0040-1951(81)90110-4
- John, B. E., and Blundy, J. D. (1993). Emplacement-related deformation of granitoid magmas, southern Adamello Massif, Italy. *Geol. Soc. Am. Bull.* 105, 1517–1541. doi: 10.1130/0016-7606(1993)105<1517:ERDOGMR>&t.3.CO;2
- Johnson, A. M., and Pollard, D. D. (1973). Mechanics of growth of some laccolithic intrusions in the Henry mountains, Utah, I. *Tectonophysics* 18, 261–309. doi: 10.1016/0040-1951(73)90050-4
- Kendrick, J. E., Lavallée, Y., Hess, K.-U., Heap, M. J., Gaunt, H. E., Meredith, P. G., et al. (2013). Tracking the permeable porous network during strain-dependent magmatic flow. *J. Volcanol. Geotherm. Res.* 260, 117–126. doi: 10.1016/j.jvolgeores.2013.05.012
- Kendrick, J. E., Lavallée, Y., Varley, N. R., Wadsworth, F. B., Lamb, O. D., and Vasseur, J. (2016). Blowing off steam: Tuffisite formation as a regulator for Lava Dome Eruptions. *Front. Earth Sci.* 4:41. doi: 10.3389/feart.2016.00041
- Kennedy, B. M., Wadsworth, F. B., Vasseur, J., Ian Schipper, C., Mark Jellinek, A., von Aulock, F. W., et al. (2016). Surface tension driven processes densify and retain permeability in magma and lava. *Earth Planet. Sci. Lett.* 433, 116–124. doi: 10.1016/j.epsl.2015.10.031
- Kerr, A. D., and Pollard, D. D. (1998). Toward more realistic formulations for the analysis of laccoliths. *J. Struct. Geol.* 20, 1783–1793. doi: 10.1016/S0191-8141(98)00071-6
- Khan, M. A. (1962). The anisotropy of magnetic susceptibility of some igneous and metamorphic rocks. *J. Geophys. Res.* 67, 2873–2885. doi: 10.1029/JZ0671007p02873
- Knight, M. D., and Walker, G. P. L. (1988). Magma flow directions in dikes of the Koolau Complex, Oahu, determined from magnetic fabric studies. *J. Geophys. Res.* 93:4301. doi: 10.1029/JB093iB05p04301
- Kushnir, A. R. L., Martel, C., Champallier, R., and Arbaret, L. (2017). In situ confirmation of permeability development in shearing bubble-bearing melts and implications for volcanic outgassing. *Earth Planet. Sci. Lett.* 458, 315–326. doi: 10.1016/j.epsl.2016.10.053
- Lavallée, Y., Hess, K.-U., Cordonnier, B., and Bruce Dingwell, D. (2007). Non-Newtonian rheological law for highly crystalline dome lavas. *Geology* 35, 843–846. doi: 10.1130/G23594A.1
- Leshner, C. E., and Spera, F. J. (2015). “Thermodynamic and transport properties of silicate melts and magma,” in *The Encyclopedia of Volcanoes*, eds H. Sigurdsson, B. Houghton, S. R. McNutt, H. Rymer, and J. Stix (Elsevier Academic Press), 113–141. doi: 10.1016/B978-0-12-385938-9.00005-5
- Lipman, P. W., Moore, J. G., and Swanson, D. A. (1981). “Bulging of the north flank before the May 18 eruption - geodetic data,” in *The 1980 Eruptions of Mount Saint Helens, Washington. Geological Survey Professional Paper 1250*, eds P. W. Lipman and D. R. Mullineaux (Washington, DC: United States Government Printing Office), 143–155.
- Marsh, B. D. (1981). On the crystallinity, probability of occurrence, and rheology of lava and magma. *Contrib. to Mineral. Petrol.* 78, 85–98. doi: 10.1007/BF00371146
- Marsh, B. D. (1996). Solidification fronts and magmatic evolution. *Mineral. Mag.* 60, 5–40. doi: 10.1180/minmag.1996.060.398.03
- Martin, E., and Sigmarsson, O. (2010). Thirteen million years of silicic magma production in Iceland: Links between petrogenesis and tectonic settings. *Lithos* 116, 129–144. doi: 10.1016/j.lithos.2010.01.005
- Martin, E., Paquette, J. L., Bosse, V., Ruffet, G., Tiepolo, M., and Sigmarsson, O. (2011). Geodynamics of rift-plume interaction in Iceland as constrained by new <sup>40</sup>Ar/<sup>39</sup>Ar and in situ U–Pb zircon ages. *Earth Planet. Sci. Lett.* 311, 28–38. doi: 10.1016/j.epsl.2011.08.036
- Martin, L. G. (2002). Insights into volcanic conduit flow from an open-source numerical model. *Geochem. Geophys. Geosyst.* 3, 1–18. doi: 10.1029/2001GC000192
- McCarthy, W., Petronis, M. S., Reavy, R. J., and Stevenson, C. T. (2015). Distinguishing diapirs from inflated plutons: an integrated rock magnetic fabric and structural study on the Roundstone Pluton, Western Ireland. *J. Geol. Soc. London* 172, 550–565. doi: 10.1144/jgs2014-067
- Merle, O., and Lénat, J.-F. (2003). Hybrid collapse mechanism at Piton de la Fournaise volcano, Reunion Island, Indian Ocean. *J. Geophys. Res. Solid Earth* 108:2166. doi: 10.1029/2002JB002014
- Michel, J., Baumgartner, L., Putlitz, B., Schaltegger, U., and Ovtcharova, M. (2008). Incremental growth of the Patagonian Torres del Paine laccolith over 90 k.y. *Geology* 36, 459–462. doi: 10.1130/G24546A.1
- Mills, R. D., Ratner, J. J., and Glazner, A. F. (2011). Experimental evidence for crystal coarsening and fabric development during temperature cycling. *Geology* 39, 1139–1142. doi: 10.1130/G32394.1
- Minakami, T., Ishikawa, T., and Yagi, K. (1951). The 1944 eruption of volcano Usu in Hokkaido, Japan. *Bull. Volcanol.* 11, 45–157. doi: 10.1007/BF02596029
- Nara, Y., Meredith, P. G., Yoneda, T., and Kaneko, K. (2011). Influence of macro-fractures and micro-fractures on permeability and elastic wave velocities in basalt at elevated pressure. *Tectonophysics* 503, 52–59. doi: 10.1016/j.tecto.2010.09.027
- Newhall, C. G., and Melson, W. G. (1983). Explosive activity associated with the growth of volcanic domes. *J. Volcanol. Geotherm. Res.* 17, 111–131. doi: 10.1016/0377-0273(83)90064-1
- Oehler, J.-F., van Wyk de Vries, B., and Labazuy, P. (2005). Landslides and spreading of oceanic hot-spot and arc shield volcanoes on Low Strength Layers (LSLs): an analogue modeling approach. *J. Volcanol. Geotherm. Res.* 144, 169–189. doi: 10.1016/j.jvolgeores.2004.11.023
- Okumura, S., Nakamura, M., Nakano, T., Uesugi, K., and Tsuchiyama, A. (2010). Shear deformation experiments on vesicular rhyolite: implications for brittle fracturing, degassing, and compaction of magmas in volcanic conduits. *J. Geophys. Res.* 115:B06201. doi: 10.1029/2009JB006904
- Okumura, S., Nakamura, M., Takeuchi, S., Tsuchiyama, A., Nakano, T., and Uesugi, K. (2009). Magma deformation may induce non-explosive volcanism via degassing through bubble networks. *Earth Planet. Sci. Lett.* 281, 267–274. doi: 10.1016/j.epsl.2009.02.036
- Paterson, S. R., Fowler, T. K., Schmidt, K. L., Yoshinobu, A. S., Yuan, E. S., and Miller, R. B. (1998). Interpreting magmatic fabric patterns in plutons. *Lithos* 44, 53–82. doi: 10.1016/S0024-4937(98)00022-X
- Paterson, S. R., Vernon, R. H., and Tobisch, O. T. (1989). A review of criteria for the identification of magmatic and tectonic foliations in granitoids. *J. Struct. Geol.* 11, 349–363. doi: 10.1016/0191-8141(89)90074-6
- Payacán, I., Gutiérrez, F., Gelman, S. E., Bachmann, O., and Parada, M. Á. (2014). Comparing magnetic and magmatic fabrics to constrain the magma

- flow record in La Gloria pluton, central Chile. *J. Struct. Geol.* 69, 32–46. doi: 10.1016/j.jsg.2014.09.015
- Petford, N. (2003). Rheology of granitic magmas during ascent and emplacement. *Annu. Rev. Earth Planet. Sci.* 31, 399–427. doi: 10.1146/annurev.earth.31.100901.141352
- Pistone, M., Caricchi, L., Ulmer, P., Burlini, L., Ardia, P., Reusser, E., et al. (2012). Deformation experiments of bubble- and crystal-bearing magmas: Rheological and microstructural analysis. *J. Geophys. Res. Solid Earth* 117, n/a-n/a. doi: 10.1029/2011JB008986
- Pistone, M., Caricchi, L., Ulmer, P., Reusser, E., and Ardia, P. (2013). Rheology of volatile-bearing crystal mushes: mobilization vs. viscous death. *Chem. Geol.* 345, 16–39. doi: 10.1016/j.chemgeo.2013.02.007
- Pistone, M., Cordonnier, B., Caricchi, L., Ulmer, P., and Marone, F. (2015). The viscous to brittle transition in crystal- and bubble-bearing magmas. *Front. Earth Sci.* 3:71. doi: 10.3389/feart.2015.00071
- Pistone, M., Cordonnier, B., Ulmer, P., and Caricchi, L. (2016). Rheological flow laws for multiphase magmas: an empirical approach. *J. Volcanol. Geotherm. Res.* 321, 158–170. doi: 10.1016/j.jvolgeores.2016.04.029
- Pistone, M., Whittington, A. G., Andrews, B. J., and Cottrell, E. (2017). Crystal-rich lava dome extrusion during vesiculation: an experimental study. *J. Volcanol. Geotherm. Res.* 347, 1–14. doi: 10.1016/j.jvolgeores.2017.06.018
- Pollard, D. D., and Johnson, A. M. (1973). Mechanics of growth of some laccolithic intrusions in the Henry mountains, Utah, II: bending and failure of overburden layers and sill formation. *Tectonophysics* 18, 311–354. doi: 10.1016/0040-1951(73)90051-6
- Prior, D. J., Boyle, A. P., Brenker, F., Cheadle, M. C., Day, A., Lopez, G., et al. (1999). The application of electron backscatter diffraction and orientation contrast imaging in the SEM to textural problems in rocks. *Am. Mineral.* 84, 1741–1759. doi: 10.2138/am-1999-11-1204
- Roni, E., Westerman, D. S., Dini, A., Stevenson, C. T. E., and Rocchi, S. (2014). Feeding and growth of a dyke-laccolith system (Elba Island, Italy) from AMS and mineral fabric data. *J. Geol. Soc. Lond.* 171, 413–424. doi: 10.1144/jgs2013-019
- Shields, J. K., Mader, H. M., Pistone, M., Caricchi, L., Floess, D., and Putlitz, B. (2014). Strain-induced outgassing of three-phase magmas during simple shear. *J. Geophys. Res. Solid Earth* 119, 6936–6957. doi: 10.1002/2014JB011111
- Silva, P. F., Marques, F. O., Machek, M., Henry, B., Hirt, A. M., Roxerová, Z., et al. (2014). Evidence for non-coaxiality of ferrimagnetic and paramagnetic fabrics, developed during magma flow and cooling in a thick mafic dyke. *Tectonophysics* 629, 155–164. doi: 10.1016/j.tecto.2014.04.017
- Smith, J. V., Miyake, Y., and Oikawa, T. (2001). Interpretation of porosity in dacite lava domes as ductile-brittle failure textures. *J. Volcanol. Geotherm. Res.* 112, 25–35. doi: 10.1016/S0377-0273(01)00232-3
- Smith, J. V., Yamauchi, S., and Miyake, Y. (1993). Microshear zones in a Miocene submarine dacite dome of southwest Japan. *Bull. Volcanol.* 55, 438–442. doi: 10.1007/BF00302003
- Snyder, G. L., and Fraser, G. D. (1963). “Pillowed lavas, I. Intrusive layered lava pods and pillowed lavas, Unalaska Island, Alaska,” in *Geological Survey Professional Paper 454-B* (Washington, DC: United States Government Printing Office), B1–B23.
- Sparks, R. S. J., Murphy, M. D., Lejeune, A. M., Watts, R. B., Barclay, J., and Young, S. R. (2000). Control on the emplacement of the andesite lava dome of the Soufriere Hills volcano, Montserrat by degassing-induced crystallization. *Terra Nov.* 12, 14–20. doi: 10.1046/j.1365-3121.2000.00267.x
- Sparks, R. S. J., Young, S. R., Barclay, J., Calder, E. S., Cole, P., Darroux, B., et al. (1998). Magma production and growth of the lava dome of the Soufriere Hills Volcano, Montserrat, West Indies: November 1995 to December 1997. *Geophys. Res. Lett.* 25, 3421–3424. doi: 10.1029/98GL00639
- Stasiuk, M. V., Barclay, J., Carroll, M. R., Jaupart, C., Ratté, J. C., Sparks, R. S. J., et al. (1996). Degassing during magma ascent in the Mule Creek vent (USA). *Bull. Volcanol.* 58, 117–130. doi: 10.1007/s004450050130
- Stevenson, C. T. E., Owens, W. H., Hutton, D. H. W. W., Hood, D. N., Meighan, I. G., and Meigan, I. G. (2007). Laccolithic, as opposed to cauldron subsidence, emplacement of the Eastern Mourne pluton, N. Ireland: evidence from anisotropy of magnetic susceptibility. *J. Geol. Soc. London* 164, 99–110. doi: 10.1144/0016076492006-008
- Stewart, A. L., and McPhie, J. (2003). Internal structure and emplacement of an Upper Pliocene dacite cryptodome, Milos Island, Greece. *J. Volcanol. Geotherm. Res.* 124, 129–148. doi: 10.1016/S0377-0273(03)00074-X
- Swanson, S. E., Naney, M. T., Westrich, H. R., and Eichelberger, J. C. (1989). Crystallization history of Obsidian Dome, Inyo Domes, California. *Bull. Volcanol.* 51, 161–176. doi: 10.1007/BF01067953
- Tuffen, H., and Castro, J. M. (2009). The emplacement of an obsidian dyke through thin ice: Hrafninnuhryggur, Krafla Iceland. *J. Volcanol. Geotherm. Res.* 185, 352–366. doi: 10.1016/j.jvolgeores.2008.10.021
- Tuffen, H., and Dingwell, D. (2005). Fault textures in volcanic conduits: evidence for seismic trigger mechanisms during silicic eruptions. *Bull. Volcanol.* 67, 370–387. doi: 10.1007/s00445-004-0383-5
- Tuffen, H., Dingwell, D. B., and Pinkerton, H. (2003). Repeated fracture and healing of silicic magma generate flow banding and earthquakes? *Geology* 31, 1089–1092. doi: 10.1130/G19777.1
- Turcotte, D. L., and Schubert, G. (2002). *Geodynamics*. Cambridge: Cambridge University Press
- van Wyk de Vries, B., Kerle, N., and Petley, D. (2000). Sector collapse forming at Casita volcano, Nicaragua. *Geology* 28, 167–170. doi: 10.1130/0091-7613(2000)28<167:SCFACV>2.0.CO;2
- van Wyk de Vries, B., Márquez, A., Herrera, R., Bruña, J. L. G., Llanes, P., and Delcamp, A. (2014). Craters of elevation revisited: forced-folds, bulging and uplift of volcanoes. *Bull. Volcanol.* 76:875. doi: 10.1007/s00445-014-0875-x
- Walker, G. P. L. (1958). Geology of the Reydarfjörður area, eastern Iceland. *Q. J. Geol. Soc.* 114, 367–391. doi: 10.1144/gsjgs.114.1.0367
- Walker, G. P. L. (1963). The Breiddalur central volcano, eastern Iceland. *Q. J. Geol. Soc.* 119, 29–63. doi: 10.1144/gsjgs.119.1.0029
- Walker, G. P. L. (1966). Acid volcanic rocks in Iceland. *Bull. Volcanol.* 29, 375–402. doi: 10.1007/BF02597164
- Walker, G. P. L. (1974). “The structure of eastern Iceland,” in *Geodynamics of Iceland and the North Atlantic Area*, ed L. Kristiansson (Dordrecht: Reidel), 177–188.
- Westrich, H. R., Stockman, H. W., and Eichelberger, J. C. (1988). Degassing of rhyolitic magma during ascent and emplacement. *J. Geophys. Res.* 93:6503. doi: 10.1029/JB093iB06p06503
- Wright, H. M. N., and Weinberg, R. F. (2009). Strain localization in vesicular magma: implications for rheology and fragmentation. *Geology* 37, 1023–1026. doi: 10.1130/G30199A.1
- Žák, J., Paterson, S. R., Janoušek, V., and Kabele, P. (2009). The mammoth peak sheeted complex, Tuolumne batholith, Sierra Nevada, California: a record of initial growth or late thermal contraction in a magma chamber? *Contrib. Mineral. Petrol.* 158, 447–470. doi: 10.1007/s00410-009-0391-8
- Žák, J., Schulmann, K., and Hroudá, F. (2005). Multiple magmatic fabrics in the Sázava pluton (Bohemian Massif, Czech Republic): a result of superposition of wrench-dominated regional transpression on final emplacement. *J. Struct. Geol.* 27, 805–822. doi: 10.1016/j.jsg.2005.01.012
- Závada, P., Schulmann, K., Lexa, O., Hroudá, F., Haloda, J., and Týcová, P. (2009). The mechanism of flow and fabric development in mechanically anisotropic trachyte lava. *J. Struct. Geol.* 31, 1295–1307. doi: 10.1016/j.jsg.2009.04.002

**Conflict of Interest Statement:** The authors declare that the research was conducted in the absence of any commercial or financial relationships that could be construed as a potential conflict of interest.

Copyright © 2018 Mattsson, Burchardt, Almqvist and Ronchin. This is an open-access article distributed under the terms of the Creative Commons Attribution License (CC BY). The use, distribution or reproduction in other forums is permitted, provided the original author(s) and the copyright owner are credited and that the original publication in this journal is cited, in accordance with accepted academic practice. No use, distribution or reproduction is permitted which does not comply with these terms.